Astron. Astrophys. Suppl. Ser. 116, 211-238 (1996)

Time variability of five strong 12 GHz methanol masers

L. Moscadelli¹ and M. Catarzi(†)²

¹ Universitá di Bologna, Dipartimento di Astronomia, via Zamboni 33, 40100, Bologna, Italy, and Istituto di Radioastronomia (C.N.R.), via Gobetti 101, 40129, Bologna, Italy

² Osservatorio Astrofisico di Arcetri, Largo E. Fermi 5, 50125, Firenze, Italy

Received December 8, 1994; accepted September 19, 1995

Abstract. — Five intense 12 GHz methanol masers with structured profile have been monitored during the period 90 Nov.—92 Apr., in order to study the variability on time scales ranging from one week to about 2 years. The integrated flux density of W3(OH), G188.94 +0.89, NGC 7538 remains constant (within the measurement uncertainties) during our period of observation. By amplitude normalization and removal of instrumental velocity shifts, we could investigate variations of flux density as small as a few per cent. For W3(OH) and G188.94+0.89, we find that the flux density varies up to a maximum of 8% over 1.5 years; for NGC 7538, we obtain an upper limit of 10% over 1.5 years. The integrated flux density of the remaining two sources, Cep A and W48, varies up to a factor of 2—3 and both show an intensity increase which varies with velocity. We could study the dependence of the intensity variation on the velocity with a precision limited only by the noise. We interpret the small time variability presented by the first three sources as due to proper motions of the maser spots. To explain the velocity dependence of the intensity variation of the two more variable sources, we suggest, for Cep A, the presence of still unsaturated emission components and, for W48, an edge-on disk configuration.

Key words: masers — ISM: HII region — ISM: molecules — radio lines: interstellar

1. Introduction

Several methanol transitions have been observed in maser emission towards star forming regions. They are catalogued in two varieties, Class I and Class II (Menten 1991a), with Class II characterized by a closer location to IR centers and UCHII regions, signposts of star forming activity. Among the Class II masers the strongest emission is observed from the transitions near 6.7 GHz (Menten 1991b) and 12.2 GHz (Batrla et al. 1987), which are almost always associated (Mac Leod et al. 1992) and likely emerging from the same molecular gas condensations (Menten et al. 1992).

Early observations of Class I and II methanol masers have demonstrated the lack of time variability over time-scales of years (Menten 1991a, Catarzi et al. 1993). This behaviour seems very peculiar compared to that of the other two intense interstellar masers: $\rm H_2O$, variable over days, and OH, variable over 1-5 years. Recently, more accurate monitoring of 12 GHz masers has revealed relative intensity variations of 15–20% over 4 years (Mac Leod et al. 1993) and for a few sources, a much more pronounced

Send offprint requests to: L. Moscadelli, Max-Planck-Institut für Radioastronomie, Auf dem Hügel 69, 53121 Bonn 1, Germany

absolute intensity variability of several 10%/week (Caswell et al. 1993) has been reported.

We have monitored five of the strongest 12 GHz sources in the northern hemisphere in order to determine their variability rate on time-scales ranging from one week to 2 years. In all of the selected sources, intense infrared emission centers (flux at 100 μ m > 100 Jy) and UCHII regions are present (Kurtz et al. 1993). Towards three of them (W3(OH), NGC 7538, Cep A) VLBI observations show that the 12 GHz masers position is coincident with that of an UCHII region (Menten et al. 1988). In order to detect minimal variations of the emission profile we have paid particular attention to the problems of amplitude normalization and removal of instrumental velocity shifts before comparing different epoch spectra. For each source, we have attempted to interpret the results of the time variability in terms of the dynamical configuration and/or the degree of saturation of the emission.

2. Observations

Single dish spectral observations were carried out in five runs, November 1990, January 1991, April 1991, October 1991 and April 1992, with the 32 m Medicina radiotelescope operated by the Istituto di Radioastronomia CNR (Bologna). At 12.2 GHz the HPBW is 2.5. The receiver

used is described by Catarzi et al. (1993) and Catarzi et al. (1990). The system temperature for each run was \approx 200 K.

Table 1 shows the observed sources together with the main characteristics of their emission, the distance and the bibliographical reference. Over the duration (3-5 days) of each run we observed each of the five sources several times. Interference from commercial satellites have heavily disturbed the observations and we could not use the spectra of NGC 7538 and Cep A for the 4/91 run and of W48 for the 10/91 one.

The flux density calibration was made by continuum observations of DR21 (20.4 Jy) and 3C286 (4.01 Jy) (Ott et al. 1994). The resulting conversion factor, average over all runs, was 0.16 K/Jy with a mean calibration error of 10% (see Table 2 for the values of each run).

The spectra were obtained using the Arcetri digital 1024 channel autocorrelator in the total power mode. We used bandwidths in the range 0.78 MHz to 6.25 MHz, corresponding to a velocity resolutions of 0.019 km s⁻¹ to 0.15 km s⁻¹. The maximum resolution of 0.019 km s⁻¹ was not available for the 11/90 run, when the autocorrelator operated with 520 channels. Generally the integration time was 5 min in the ON and OFF positions, resulting in a mean rms noise level in the difference spectra between ≈ 1.5 Jy and ≈ 4.4 Jy, depending on the bandwidth.

To reduce and analyze the spectra we used CLASS, the reduction package developed at the IRAM (Grenoble), the flexibility and potential of which has greatly facilitated the operations on spectra requested by our analysis. After calibrating spectra in Jy, we removed a polynomial baseline. Generally a polynomial of order ≤ 3 resulted sufficient to get the baseline flat.

3. Description of the analysis

A comparison of spectra from the first and last observing run is presented in Fig. 1. One can note that the emission profiles do not seem to have changed during the 18 month interval.

In order to determine the time variability of the emission by comparing several spectra of a source, one has to take in account:

- 1. The uncertainty in the calibration of flux densities due to atmospheric fluctuations and telescope pointing errors. For every run we estimated the uncertainty of the conversion factor from K to Jy by the mean dispersion of the single measurements around the calibration curve in the "conversion factor/elevation" plot. Table 2 shows the mean conversion factor, the mean dispersion and the percent calibration error for each run.
- 2. If the emission is extended with respect to the telescope beam, the relative intensities of spatial components are influenced by the telescope pointing repeatability. We have mapped the three sources with

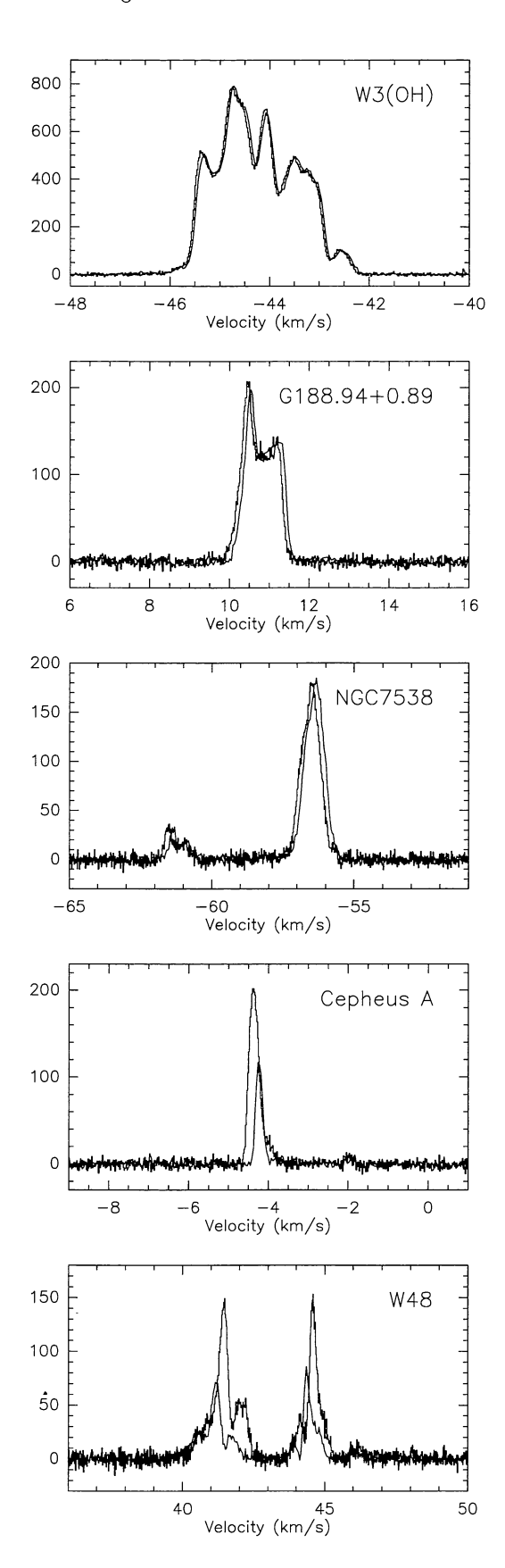


Fig. 1. For each of the five sources the spectrum of the 4/92 run (histogram plot) is shown on the top of the 11/90 one (normal plot). The flux density scale is in Jy

Table 1. Observed sources

Sources	α (1950)	$\delta~(1950)$	Vel. range [†]	Peak intensity [‡]	Distance	Ref.
	(h m s)	(° ′ ″)	$({\rm km\ s^{-1}})$	(Jy)	(kpc)	
W3(OH)	02 23 16.4	61 38 57.7	-46.0, -42.0	800	2.2 (5)	7
G188.94+0.89	06 05 53.7	21 39 09	+10.0, +11.5	183	2.2 (4)	6
NGC 7538	23 11 36.5	61 11 47	-62.0, -55.5	203	$2.8 \pm 0.9 \ (1)$	6
Cep A	22 54 27.0	61 45 46	-4.5, -1.5	95	0.725(3)	6
W48	18 59 12.8	01 09 13	+39.5, +47.0	102	3.2 ± 0.8 (2)	6

† 0.5 km s⁻¹ approximate values.

- ‡ From 1/91 scans (0.019 km s⁻¹ resolution); the calibration error is estimated to be 9.4%.
- 1. Crampton et al. (1978)
- 2. Downes et al. (1980)
- 3. Garmany (1973)
- 4. Kömpe et al. (1989)
- 5. Humphreys (1978)
- 6. Koo et al. (1988)
- 7. Menten et al. (1988)
 - a more structured spectrum (W3(OH), G188.94+0.89 and W48) with five-points grid (R.A. and Dec. offset = 1/2 beam) to evaluate the variations of the emission profile due to pointing errors.
- 3. Errors due to the polarization of the radiation. To avoid the effect, all spectra were taken using left circular polarization.
- 4. The width and the position of the spectral resolution elements, that influence the spectral profile in the case of low velocity resolution. The lowpass filter at the input of the autocorrelator, that determines the observational bandwidth, defines the width of the velocity resolution element and can also affect the spectral profile with its ripples. In order to investigate the time variation of the spectral profile, we used only spectra with the highest resolution (0.019 km s^{-1}), obtained with the same 0.78 MHz lowpass filter at the input of the digital autocorrelator. Considering that the narrowest line in our spectra has a FWHM of ≈ 0.2 km s^{-1} , we have verified that, at our highest resolution, a different central velocity between the spectra causes intensity variations that are negligible in comparison with the noise level.

The different resolution and central velocity does not affect integrated quantities as the total flux density (Jy km s^{-1}) and the first moment of the emission velocity

(km s⁻¹). Our analysis consists of two steps. First, using all spectra available for a source, we study the time variability of the integrated flux density and the first moment of the emission velocity. Using only spectra with 0.019 km s⁻¹ resolution (the period 1/91 - 4/92) we analyse the time variability of the spectral profiles.

4. Time variability of the integrated flux density

The integrated flux density is calculated adding all channels with emission. The error due to the spectral noise, σ_n , is always less or much less than the calibration error, $\sigma_{\rm cal}$ (calculated by means of the percent error, given, for each run, in the last column of Table 2). We note that for each source and for every run the dispersion of the integrated emission is within the calibration error. So small variations in the source emission on a time scale of a few days (the duration of a run) are completely masked by the observational uncertainties.

For every run, we have calculated the weighted mean of the values of each source, using as weight the total error, $\sigma_{\rm tot}$, of each observation, $\sigma_{\rm tot} = \sqrt{\sigma_{\rm n}^2 + \sigma_{\rm cal}^2}$.

In Fig. 2 we present the plots of the mean integrated flux density against time for each source. For W48, which shows two groups of emission components separated in velocity (see Fig. 1), we have also studied the time variation of the integrated emission of each group. From these plots it is clear that:

- 1. The integrated flux density of the sources W3(OH), G188.94+0.89 and NGC 7538, has remained constant (within $\sigma_{\rm tot} \approx$ our calibration error of 9–14%) on a time scale of 18 months. In Table 3 we give the mean value of the integrated flux density of these sources over the whole observation period (weighted mean of the values of the single runs).
- 2. The integrated emission of Cep A and W48 has increased during the time of our observations. Cep A has changed from ≈ 24 Jy km s⁻¹ to ≈ 68 Jy km s⁻¹ and W48 from ≈ 94 Jy km s⁻¹ to ≈ 189 Jy km s⁻¹.

Table 2. The mean conversion factor

	Mean conversion	Mean	Calibration		
Run	factor	${\rm dispersion}^{\dagger}$	error		
	(K/Jy)	(K/Jy)	(%)		
11/90	0.16	0.015	9.4		
1/91	0.16	0.015	9.4		
4/91	0.16	0.015	9.1		
10/91	0.14	0.02	14		
4/92	0.16	0.02	12		

[†] rms scatter about mean value.

Table 3. The mean integrated flux density

	Mean integrated				
Sources	flux density				
	$(Jy \text{ km s}^{-1})$				
W3(OH)	1405 ± 143				
G188.94+0.89	160 ± 16				
NGC 7538	184 ± 20				

5. Time variability of the first moment of the emission velocity

The first moment (f.m.) of the emission velocity is the mean of the emission velocities weighted by the corresponding flux densities. We note that, for a given source and observing run, the dispersion of the f.m. is in most cases much larger than the error due to the spectral noise and the velocity sampling, $\sigma_{\rm ns}$. The random nature of the distribution of the values can be explained by the presence of another kind of error, $\sigma_{\rm ir}$, resulting from the combined action of instrumental velocity shifts (inaccuracy in the calculation of the observing frequency and, also, instability of the frequency conversion system) and effects introduced by the reduction process (for instance, baseline subtractions). In the section "first moment error estimation", we give the procedure used to estimate $\sigma_{\rm ir}$.

For every run we have calculated the weighted mean of the f.m., weighting by the total error of each observation, $\sigma_{\rm tot} = \sqrt{\sigma_{\rm ns}^2 + \sigma_{\rm ir}^2}$.

Table 4. The systematic velocity shift

Systematic			
velocity shift			
$(\mathrm{km}\ \mathrm{s}^{-1})$			
$+0.002 \pm 0.017$			
$+0.017\pm0.009$			
-0.076 ± 0.014			
$+0.217\pm0.019$			
-0.057 ± 0.015			

In Fig. 3a we give the plots of the f.m. of the emission velocity against time for all sources excepting W48. One can see that the f.m. varies with time in a very similar way: the value of the 10/91 run is always higher than the other values, the range of dispersion of which is fairly consistent with the errors. The similar trend for the different sources is an indication that all spectra of a given run, particularly of the 10/91 one, are affected by a systematic (instrumental) velocity shift. In order to determine it, for each of the four sources, we calculate the difference between the value of a given run and the weighted mean over all runs (the 10/91 one, most affected by the systematic error, excluded) and then we take the weighted mean of the differences. The results are shown in Table 4. In Table 5 we give the mean values (weighted mean over all runs, 10/91 excluded) of the f.m. for the four sources.

In Fig. 3b we present the plots of W48 (pertaining to the total emission and to each of the two distinct groups of spectral components) corrected for the known systematic error.

We conclude that:

1. The first moment of the emission velocity of W3(OH), G188.94+0.89, NGC 7538 and Cep A remains constant

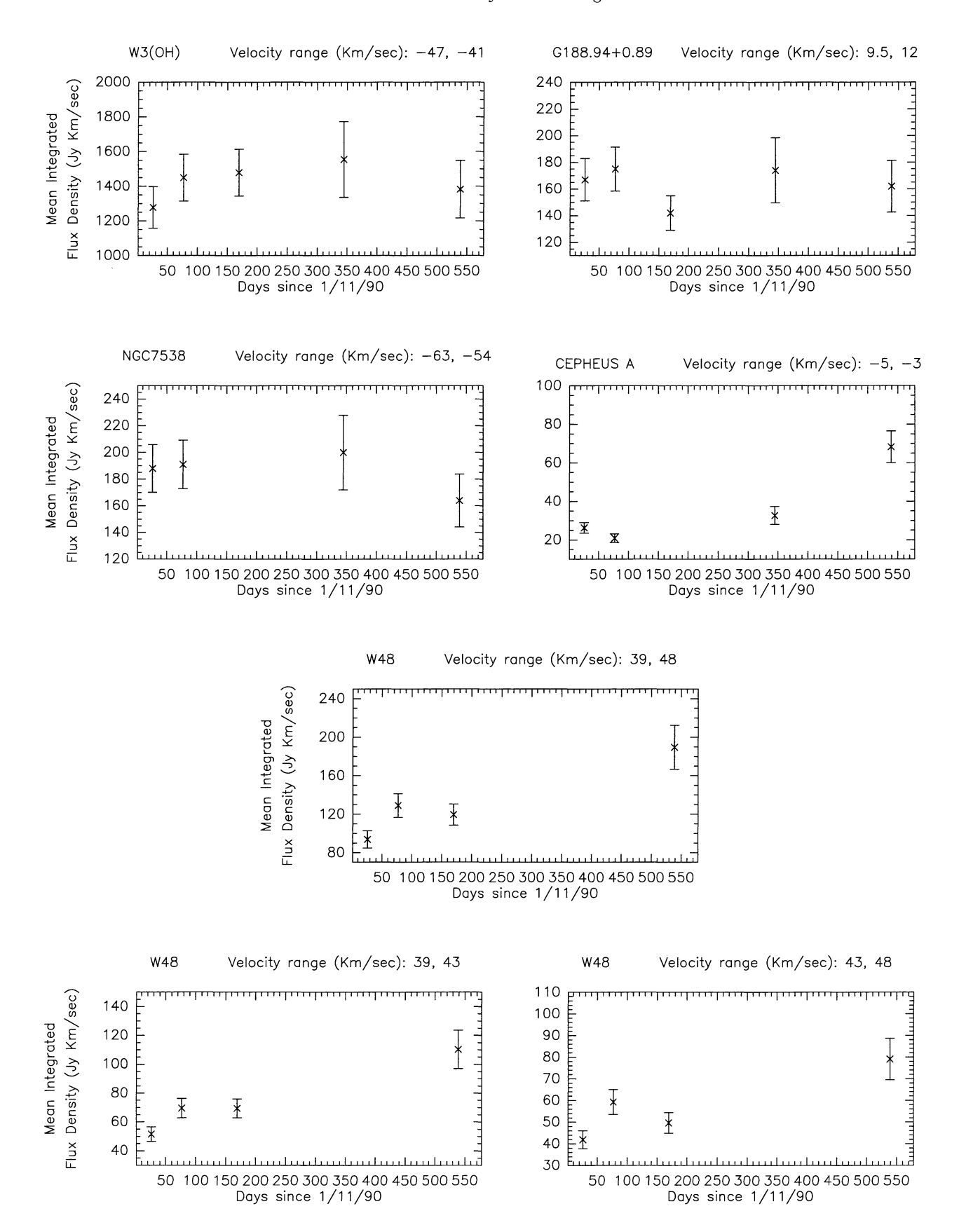


Fig. 2. Plots of the mean integrated flux density against time. For each source we indicate the velocity range over which the emission has been integrated. For W48, the plots corresponding to both the whole emission and each of the two sections of spectral components, are shown. Error bars represent the rms uncertainty of the mean value

Table 5. The mean first moment of the emission velocity

~	Mean velocity
Sources	first moment
	$({\rm km\ s^{-1}})$
W3(OH)	-44.223 ± 0.007
G188.94+0.89	$+10.807 \pm 0.006$
NGC 7538	-56.991 ± 0.045
Cep A	-4.284 ± 0.035

(after correcting for the systematic shift) over our observation period of 18 months.

2. The first moment of the emission velocity of both groups of spectral components of W48 shows a continuous increase during the 18 months. For the first group of components we find an increase of about $0.44~\rm km~s^{-1}$, for the second this is about $0.28~\rm km~s^{-1}$.

6. Time variability of the spectral profile

6.1. Description of the analysis

With two spectra of the same source taken at two different epochs, t_1 and t_2 , one can study the variation of the spectral profile by examinating the flux density ratio, $R_{12}(v)$:

$$R_{12}(v) = \frac{F_2(v)}{F_1(v)} \quad t_1 < t_2$$

where $F_i(v)(i = 1, 2)$ is the flux density at velocity v observed at the epoch t_i .

However, the normalization of the flux density scale and the removal of eventual velocity shifts must be considered first.

In order to normalize the flux density scale for spectra from the same run, we demand that the integrated flux density be equal to the mean value of the run. Since within the same run one can assume that the intrinsic variation of the integrated flux density is much less than the error due to the calibration (see Sect. 4), with this normalization, the flux density ratio is no longer affected by the calibration uncertainty. We shall discuss this last point in more detail below.

The measured flux density, F(v), and integrated flux density, I, of a spectrum are both affected by the calibration uncertainty representable as a multiplicative

factor G:

$$F(v) = GF^t(v)$$

$$I = GI^t$$

where the t superscript indicates the true values.

If we normalize two spectra, 1 and 2, by requiring that $I_1 = I_2$, then we multiply $F_1(v)$ by the factor I_2/I_1 . This factor can be expanded in the following way:

$$\frac{I_2}{I_1} = \frac{G_2 I_2^t}{G_1 I_1^t} = 1 + \frac{\Delta G}{G_1} + \frac{\Delta I^t}{I_1^t} + \frac{\Delta G \Delta I^t}{G_1 I_1^t}$$

where $\Delta I^t = I_2^t - I_1^t$ and $\Delta G = G_2 - G_1$ represent the intrinsic variation of the integrated flux density and the calibration fluctuation respectively.

Neglecting the 2° order term, if $\frac{\Delta I^t}{I_1^t} \ll \frac{\Delta G}{G_1}$, then

$$\frac{I_2}{I_1} \approx 1 + \frac{\Delta G}{G_1} = \frac{G_2}{G_1}$$

So, after the normalization, the ratio between the flux densities becomes,

$$R_{12}(v) = \frac{F_2(v)}{F_1(v)G_2/G_1} = \frac{F_2^t(v)G_2}{F_1^t(v)G_1G_2/G_1} = \frac{F_2^t(v)}{F_1^t(v)}$$

and is effectively free from calibration errors.

From the previous analysis it is known that the integrated flux density of the three sources W3(OH), G188.94+0.89, NGC 7538 remains constant during the whole period of observation, i.e. its intrinsic variation is less than the calibration uncertainty. Then we normalize spectra of different runs requiring that their integrated flux density is equal to the mean value over all runs, shown in Table 3.

For Cep A and W48, whose integrated flux density varies much more than the calibration uncertainty, spectra of different runs are normalized equalizing the intensity of the emission peak. After this normalization, the ratio of the flux densities between two spectra is given by:

$$\frac{F_2(v)}{F_1(v)F_2(p)/F_1(p)} = \frac{F_2^t(v)/F_1^t(v)}{F_2^t(p)/F_1^t(p)}$$

where $F_i(p)(i=1,2)$ indicates the peak value.

So we can evaluate the peak-relative variation at any velocity v, without being affected by calibration errors.

For spectra from a single run we require that the first moment of the emission velocity is equal to the mean value of the run. For W3(OH), G188.94+0.89, NGC 7538, and Cep A, whose first moment remained constant over the whole observational period, we equalized the first moment of each spectrum to the mean value over all runs (shown in Table 5).

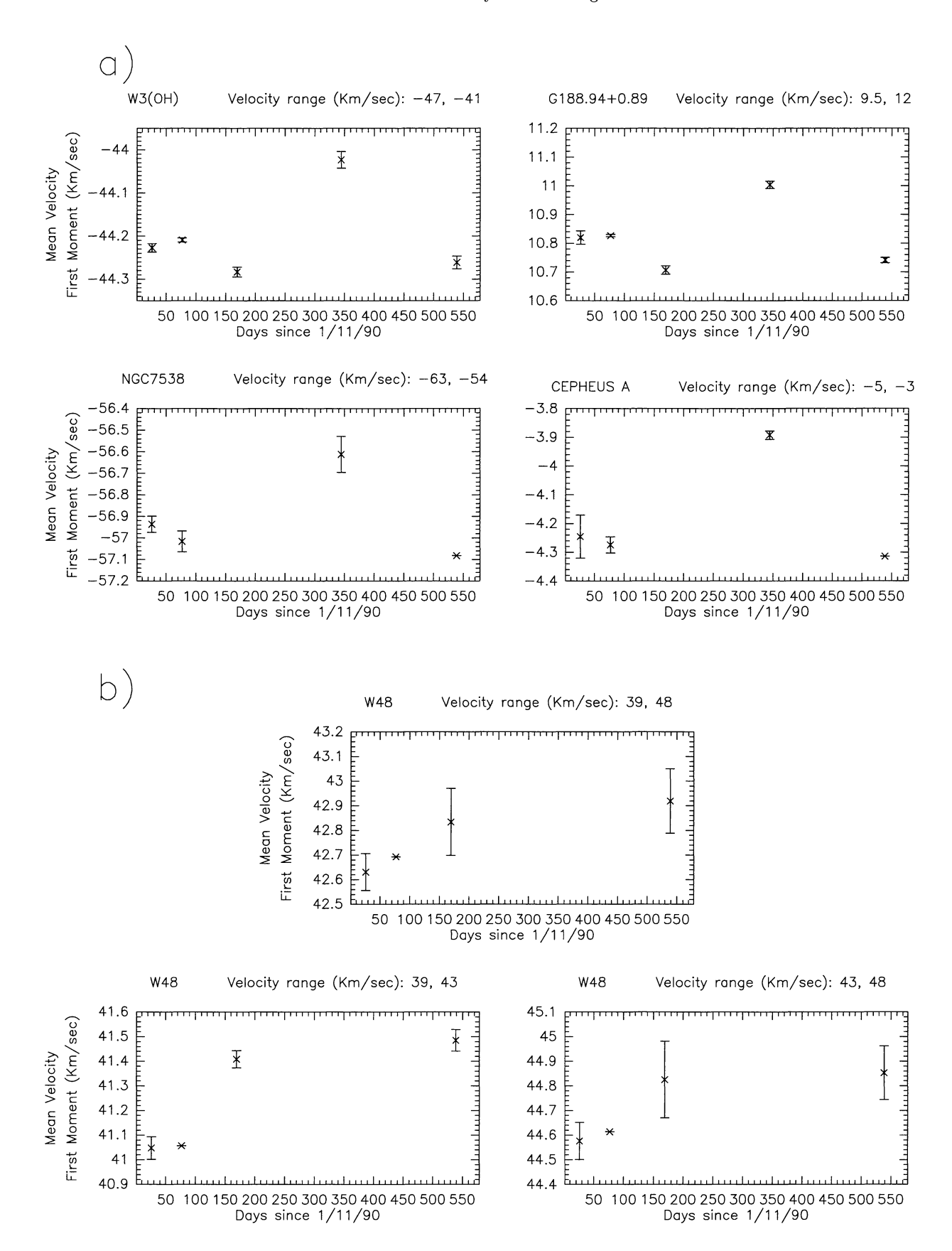


Fig. 3. Plots of the mean first moment of the emission velocity against time. a) Plots of all sources excepting W48 are shown. For each source we indicate the velocity interval used to calculate the first moment. Error bars represent the maximum value between the dispersion around the mean and the rms of the errors due to the spectral noise and the velocity sampling. b) Plots of W48 corrected for the systematic velocity shift. The upper plot is for the whole emission range, the lower ones are for each of the two sections of spectral components

Equalizing first moments of spectra is insufficient to completely remove velocity shifts. A better technique is to minimize the difference of two spectra. For each run we select the spectrum with the best signal-to-noise ratio as reference; the other spectra of the run are iteratively shifted in velocity (in steps of 0.2 of the channel width) and the reference spectrum is subtracted until finding the position for which the residual for every emission peak is minimal. If the spectrum is a blend of several peaks, it is possible with this procedure to reveal small relative variations in velocity and intensity. If the spectrum shows an isolated peak, this technique implicitly assumes that the peak position has not varied.

In Fig. 4 an example of residual minimization for the source W3(OH) is shown. The compared spectra belong to the same run and the "best" residual does not show any feature, either positive or negative, emerging above the spectral noise. The precision with which is possible to determine the position resulting in the minimum residual is strongly dependent on the signal-to-noise ratio of the spectra; in the case of W3(OH) the error is 0.2 channels only, or $0.004~\rm km~s^{-1}$.

6.2. Time variability on a time scale of a week

For each source we compared spectra of a single run using the procedure described above, and in all cases it was possible to find a relative position between the spectra (with an error < 0.4 channels) such that there are no residuals above the noise. Hence we conclude that, within the noise, the emission profiles of these sources are constant on a time scale of a week. In Table 6 we show for each source the upper limit of the percent variation of the peak flux density for each run.

During the 4/92 run we made five point maps of the sources W3(OH), G188.94+0.89, and W48. The excellent overlap of the five spectra indicates that the emission profile is the same for the 5 points of the map; hence we deduce that, for all the three sources, the area of scattering of the maser spots is point-like for our 2'.5 beam. High resolution observations towards W3(OH) (Menten et al. 1988) and G188.94+0.89 (Norris et al. 1988) have shown that the angular diameter of the cluster of masers is $\approx 1.3''$ and $\approx 0.1''$ respectively. So far no interferometric observations have been performed towards W48.

6.3. Time variability on a time scale of years

The stability of the spectral profile within each run allow us to compute the mean spectrum taking the spectral noise-weighted mean of all the spectra of the run shifted to the position of maximum overlap. Then, again using the technique of minimization of the residual, we compare the mean spectra of different runs in order to investigate variability on a time scale of months and years.

In Figs. 5-9 the results of the comparison among the several runs are shown for each source. The best overlap between the spectra with the corresponding minimum residual, an enlargment of the same residual and the ratio between the flux densities per channel are presented. As reference run, in general, we have chosen the first one (1/91) in order to find out eventual systematic time variations.

In the following we discuss the results for each source separately.

1) W3(OH)

The spectral profile does not present any variation during the period 1/91-4/91 (Fig. 5a). After about 9 months (1/91-10/91 (Fig. 5b)) some modification appears and it grows steadily until the 4/92 run (Fig. 5c) as demonstrated by the comparison of both the residual and the flux density ratio plots. The time variability occurs for two separate velocity intervals. The first, from -45.7 km $\rm s^{-1}$ to $-44.75~\rm km~s^{-1},$ corresponds to the first (lowest velocity) peak and the valley between the first and the second peak; the second, from -44.4 km s^{-1} to -43.8 kms⁻¹, corresponds to the valley between the second and the third peak and to the third peak (with a maximum variation of the flux density of about 6% at -43.95 km s⁻¹). In each of the two velocity intervals the spectral profile modification appears as a positive and a negative change in contiguous velocity spans; considering the two velocity intervals, these spans are displaced almost symmetrically with respect to the second peak.

Many individual maser spots can contribute to the emission at a single velocity. Thus, it is difficult to make definite conclusions about individual spots without interferometric observations. A single maser spot can contribute to the variability by changing both its velocity and its intensity. The kind of spectral variation found in W3(OH) suggests that the observed effect may be due to a velocity drift of several maser spots. In particular, in our case, two distinct groups of maser spots, emitting at velocities near the second peak, could be drifting in opposite directions.

Menten et al. (1992), comparing VLBI maps at 6.7 GHz and 12 GHz, have pointed out the possibility of proper motions for the methanol maser spots in agreement in magnitude and orientation with those measured for the OH maser spots by Bloemhof et al. (1992). The measured modifications of the spectral profile could reflect the change of radial velocity with position. According to the cometary bow shock pattern suggested by the observations of Bloemhof et al. (1992), methanol maser spots should be moving within the shell of shocked molecular gas present around the HII region, along a parabolic path, with a velocity increasing with the distance from the vertex. If we assume that the line of sight towards W3(OH)

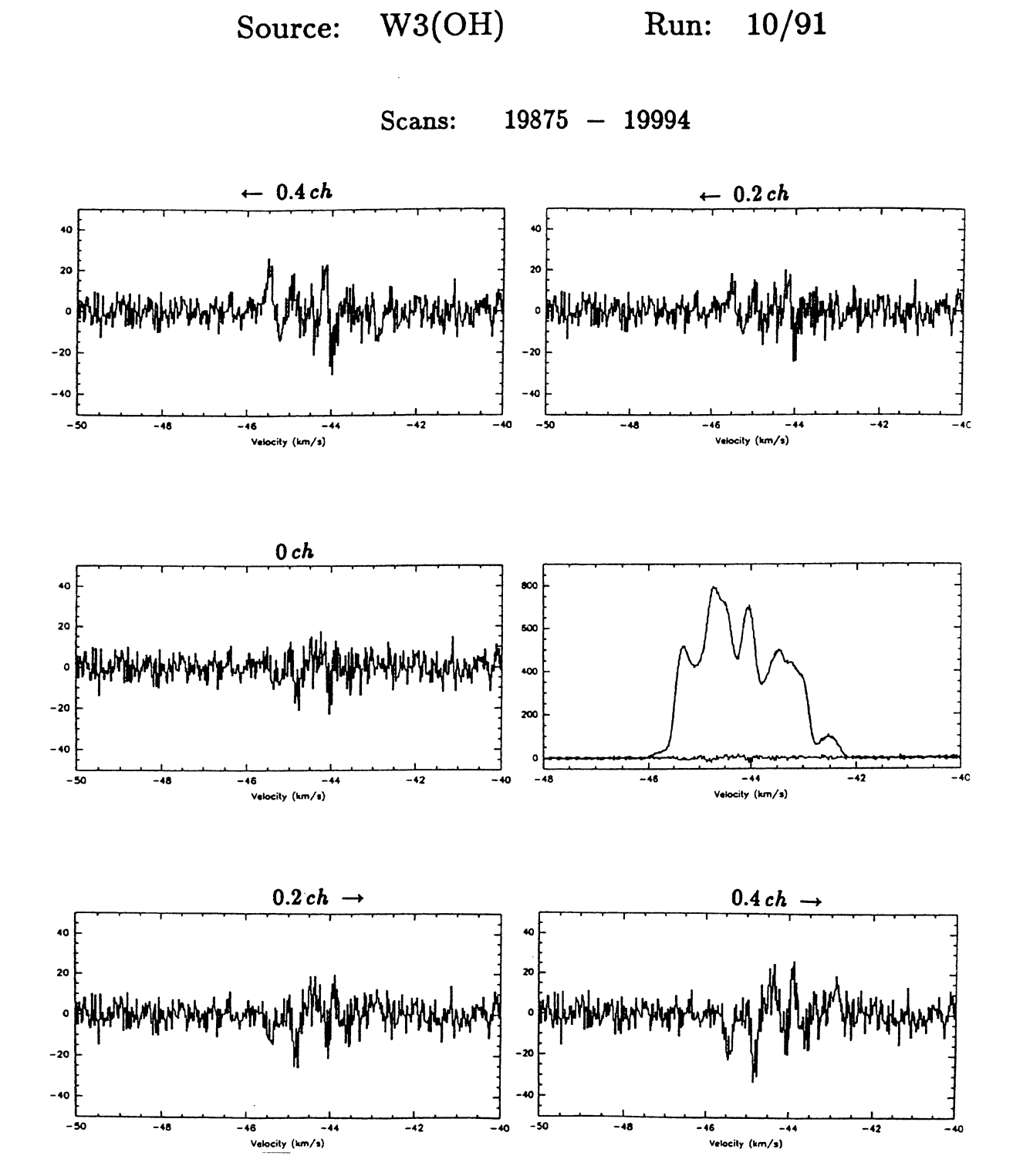


Fig. 4. Example of the residual minimization technique. For W3(OH) two spectra [scan 19875 and scan 19994 (the reference one)] of the 10/91 run are compared. The right plot in the middle shows the best overlap of the two spectra together with the corresponding minimum residual. The other plots show the residual obtained when the 19875 scan is shifted in velocity from the position of minimum residual by the indicated number of channels (the arrows indicate the direction of the shift). The flux density scale is in Jy. Note that the residuals corresponding to shifts to left are characterized by positive peak (preceding) negative dip (following) couples, while the order appears inverted (dips precede peaks) for shifts to right: this changing in the disposition of peaks and dips helps in determining the minimum residual accurately. For the high signal-to-noise ratio spectra of W3(OH), our analysis is sensitive to a velocity shift as small as 0.2 ch or 0.004 km s⁻¹

Sources	W3(OH)	G188.94+0.89	NGC 7538	Cep A	W48	
Run					1°†	2°†
1/91	2.2%	9.1%	9.1%	20.3%	19.6%	20.1%
4/91	5.2%	11.2%	‡	‡	18.6%	20.8%
10/91	4.5%	8.9%	· 10.1%	12.6%	‡	‡
4/92	4.3%	17.8%	10.3%	8.8%	27.6%	26.7%

Table 6. The upper limit of the percent variation of the peak flux density

† For W48, the values of both the 1° and the 2° (in order of increasing velocity) emission peak are presented.

is perpendicular to the axis of the bow shock¹, then maser spots moving along the far and the near side of a parabolic section of the shell, would produce intensity variations on opposite sides of the velocity at the vertex, where, in our model, the second, higher peak should originate.

We can estimate the expected proper motions on the basis of the observed velocity drift. From the flux density ratio plot of Fig. 5c, we can evaluate the 1/91 and 4/92 radial velocity of the maser spots respect to the vertex by means of the centroids of the velocity spans corresponding respectively to the negative and the positive variation. The maser spots moving along the far side of the shell (higher radial velocity) vary their velocities from $0.30 \, \mathrm{km \ s^{-1}}$ (1/91) to $0.65 \, \mathrm{km \ s^{-1}}$ (4/92). Using the equations given by Van Buren et al. (1990) for the shape of the bow shock near the vertex and the tangential flow velocity in the shell, we derive the equation that relates the displacement parallel to the axis of the bow shock, y, to the tangential flow velocity v (that, in our model, is just the radial velocity):

$$y = \frac{27}{16} \frac{l}{v_{+}^2} v^2$$

where l is the stand-off distance of the terminal wind shock from the star and v_{\star} is the velocity of the bow shock through the molecular cloud.

Using the standard values of Van Buren et al. (1990), $l = 5.5 \ 10^{16} \ {\rm cm}$, $v_{\star} = 10 \ {\rm km \ s^{-1}}$, and a distance to W3(OH) of 2.2 kpc, we find that the observed velocity drift corresponds to an angular displacement of 10 mas, that, over the period 1/91-4/92, implies a proper motion of

8 mas/year. At 12 GHz the angular resolution of transatlantic VLBI (or even VLBA) observations is better than 1 mas. So, further VLBI 12 GHz observations should allow us to measure the maser spot proper motions and to test the bow shock assumption.

2) G188.94+0.89

The spectral profile of the emission, unchanged during the period 1/91-4/91 (Fig. 6a), shows a maximum increase of about 8% at 11.22 km s^{-1} in the 10/91 spectrum (Fig.6b). The comparison of 1/91 and 4/92 spectra (Fig. 6c) shows the presence of changes in two distinct velocity intervals, in both cases with a maximum increase of 8%: one corresponds to the emission peak at 10.6 km s^{-1} , the other is centered at 11.1 km s^{-1} , at a slightly lower velocity than that at which variation is observed in the 10/91 spectrum.

So far, only one interferometric observation (Norris et al. 1988) is published for G188.94+0.89; this map shows that the maser spots are distributed in an arc, with the maximum of the radial velocity at the vertex and a continuous decrease of the velocity with increasing distance from the vertex. This is just what one would expect if one were looking at a bow-shock pattern with a line of sight sufficiently close to the bow-shock axis to see each maser spot within the paraboloidal shell moving towards us. Therefore, also in this case, the observed small variability of the spectral profile could arise just from proper motions of the maser spots along the parabolic structure of the bow-shock.

3) NGC 7538

For this source the 1σ -error of the flux density ratio is 3-4 10^{-2} , appreciably more than for G188.94+0.89 (2 10^{-2}), and for W3(OH) (0.5-1 10^{-2}). From the comparison of the 10/91 (Fig. 7a) and the 4/92 (Fig. 7b) spectra with the 1/91 one, it is evident that the flux density ratio always remains within 3σ from unity. We conclude that the spectral profile of NGC 7538 can have varied at most

[‡] No useful spectra for the run

¹Such a hypothesis is confirmed by the observations of Forster et al. (1990), who find no difference in $v_{\rm LSR}$ between the HII region and the near molecular envelope in W3(OH), while for the other HII regions of their sample the hydrogen recombination line emission occurs at a velocity offset with respect to the molecular lines of typically $\pm 6 \text{ km s}^{-1}$.

within our 3σ -error of 10% over the whole observational period, 1/91-4/92. One should note that such a signal-to-noise ratio would have made it impossible to reveal the variations found in W3(OH), while those of G188.94+0.89 would have been just detectable. Therefore it is likely that NGC 7538 is not at all peculiar and that a rate of variability of few per cent/year exists. So far, no map of the 12 GHz maser emission towards NGC 7538 is available in the literature.

4) Cep A

In Table 7 the velocity and the flux density of the emission peak of the mean spectrum of each run are reported. We can reasonably assume that the position of the peak has remained unvaried during the whole period of observation. Therefore, in order to align two spectra in velocity, as described previously, we equalize the peak intensity and look for the relative position of maximum overlap by minimizing the residual.

In the period 1/91-10/91 the peak intensity has increased by a factor of 1.44 ± 0.34 , while during the period 1/91-4/92 the rise has been by a factor of 2.10 ± 0.46 . The large relative errors are due to the calibration uncertainty. During 1/91-10/91 (Fig. 8a) the increase in intensity has been largely uniform at all velocities. The residual shows two very weak emission features in the velocity range [–5 km s⁻¹, –4 km s⁻¹] nearly completely hidden in the noise. In contrast, in the residual of the 1/91-4/92 comparison (Fig. 8b), the two features are very evident above the noise at –4.48 km s⁻¹ and –4.17 km s⁻¹ respectively. As attested by the 1/91 to 4/92 flux density ratio, on both sides of the peak, in the two ranges [–4.58 km s⁻¹, –4.34 km s⁻¹] and [–4.34 km s⁻¹, –3.80 km s⁻¹], the intensity has increased more than at the peak velocity.

In the following discussion we assume that the cause of the time variability of the emission of different maser spots is a common one. Then the time variation of the same physical parameter results in a larger intensity variation under unsaturated conditions.

The uniform increase, respect to the velocity, of the flux density during the period 1/91-10/91 can be explained assuming that the maser emission is saturated at all velocities, or that the contribution of eventual unsaturated components is negligible. The profile of the emergent intensity of a saturated maser is determined by the line profile and it remains unalterated even if the central intensity changes because of a variation, for example, of the pump rate or the amplification path length. The approximatively Gaussian shape of the 1/91 and 10/91 spectra suggests that we are seeing the emission of a single maser spot. The FWHM of both spectra is $\approx 0.20 \text{ km s}^{-1}$ and, if interpreted as Doppler broadening, corresponds to a kinetic temperature, $T_{\rm K}$, of ≈ 30 K. By comparison, the radiatively pumped model of Class II methanol masers of Cragg et al. (1992) finds that, in the presence of a source of continuum radiation warmer than the gas kinetic temperature (for istance an UCHII region), the 12 GHz and 6.7 GHz masers occur for $T_{\rm K}$ in the range 10–50 K and $N_{\rm H_2}$ (the numerical density of $\rm H_2$) in the range $10^2-10^5~\rm cm^{-3}$.

Now we try to establish if the emission of Cep A is saturated or not.

The condition for saturation is given by the inequality:

$$\frac{\Omega}{2\pi} \frac{k}{h\nu_o} T_b A > \Gamma \tag{1}$$

where Ω is the solid angle of the maser beam, $T_{\rm b}$ is the brightness temperature, A is the Einstein coefficient of spontaneous emission, Γ is the loss rate from the maser levels, ν_o is the rest frequency of the emission, k and h are respectively the Boltzmann and Planck constants. $T_{\rm b}$ can be expressed using the Rayleigh-Jeans law:

$$T_{\rm b}({\rm K}) = \frac{c^2}{2\nu_s^2 k} \frac{Fd^2}{\pi l^2} = 0.699 \, 10^{-7} \frac{d^2}{l^2} F(Jy)$$

where F is the flux density (in Jy), d is the distance to the source, l is its radius, c is the velocity of light.

In order to estimate an upper limit for the minimum flux density, F_S , needed for saturation, we use the following values of the parameters (if the value of the parameter is poorly known, we take either the maximum or the minimum value in its range of variation so as to obtain an upper limit for F_S):

$$d = 0.725 \; \text{kpc}$$

$$A = 810^{-9} \,\mathrm{s}^{-1}$$
 (Lees R.M. 1973)

$$\Omega = \pi \theta_m^2 = \pi 10^{-4} \, \mathrm{sterad}$$

(The beaming angle θ_m is estimated to be in the range $10^{-2} - 10^{-1}$ rad)

$$l = 10^{14} \, \mathrm{cm}$$

[Toward W3(OH) individual maser spots have an observed FWHP less than 7×10^{13} cm (Menten et al. 1988)]

The loss rate Γ is of the same order as the collision rate:

$$\Gamma = 10^{-10} N_{\rm H_2} \ ({\rm cm}^{-3}) \, {\rm s}^{-1}$$

On the basis of theoretical analyses of the emission mechanism of both Class II methanol masers (Cragg et al. 1992) and OH masers (Cesaroni & Walmsley 1991), which are found in the same regions as Class II methanol masers, we can estimate a reasonable upper limit for $N_{\rm H_2}$ to be 10^7 cm⁻³, implying an upper limit $\Gamma = 10^{-3}$ s⁻¹.

Inserting these values in the relation 1 we derive $F_{\rm S}$ = 70 Jy. Considering that this value is an upper limit and that it is lower than the 1/91 emission peak of 95 Jy, the hypothesis that on that date the Cep A emission was saturated is an acceptable one.

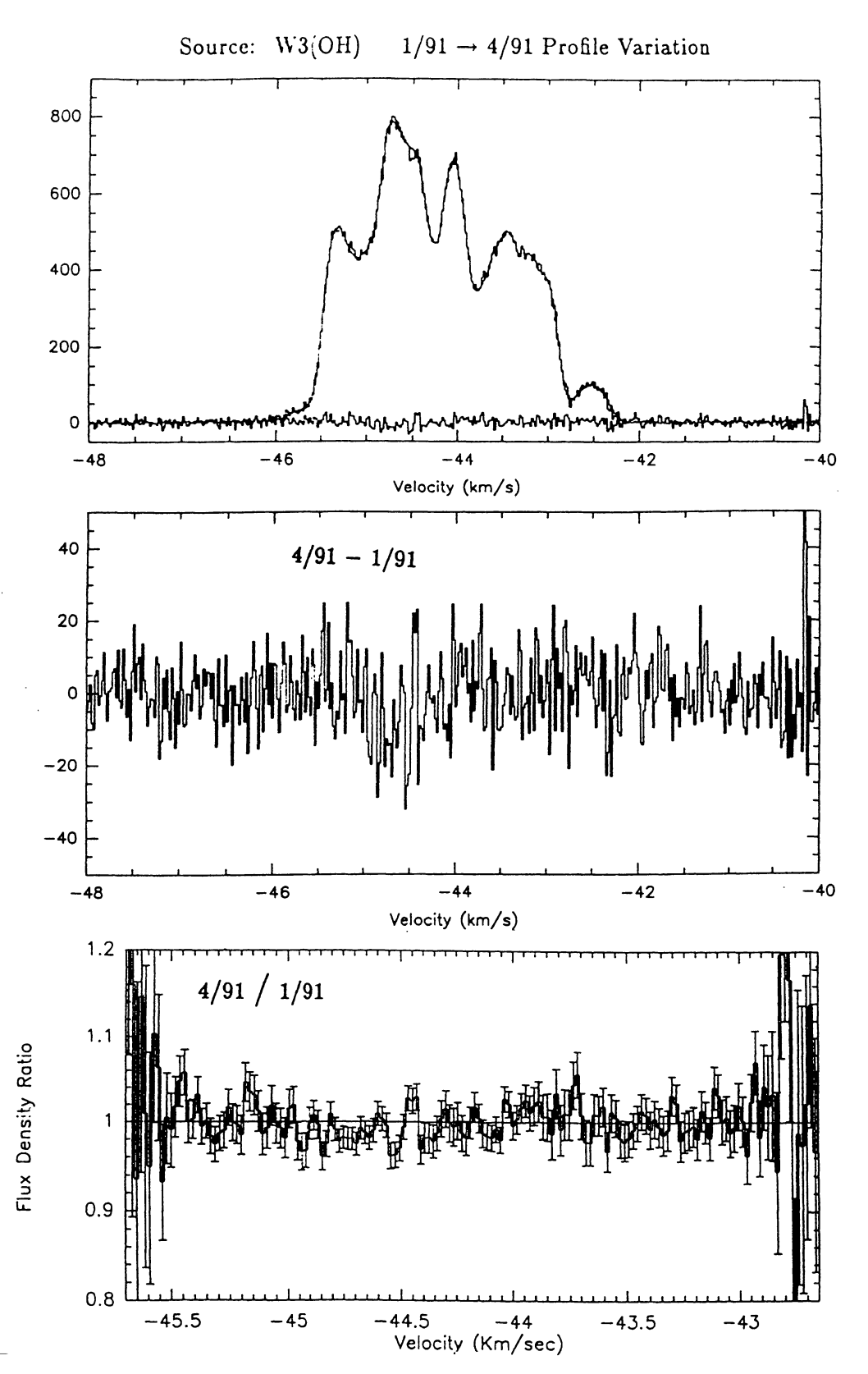


Fig. 5. - 9. 5a) For each source the results of the comparison between the mean spectra of different runs are presented. For the sources W3(OH), G188.94+0.89, NGC 7538 and Cep A, we chose as reference the first useful 1/91 run and compare the 1/91 mean spectrum with that of all the other runs. For W48, we use the 4/91 mean spectrum as the reference one, because of the best signal-to-noise ratio. In each figure, for the indicated source and pair of runs, we present: at the top, the best overlap between the spectra with the corresponding minimum residual; in the middle, an enlargment of the same residual; at the bottom, the ratio between the flux densities of the two mean spectra. The difference and the ratio between the runs reported respectively on the residual and the flux density ratio plots, indicate the order in which the runs were taken to perform the operation. See the end of caption on following page

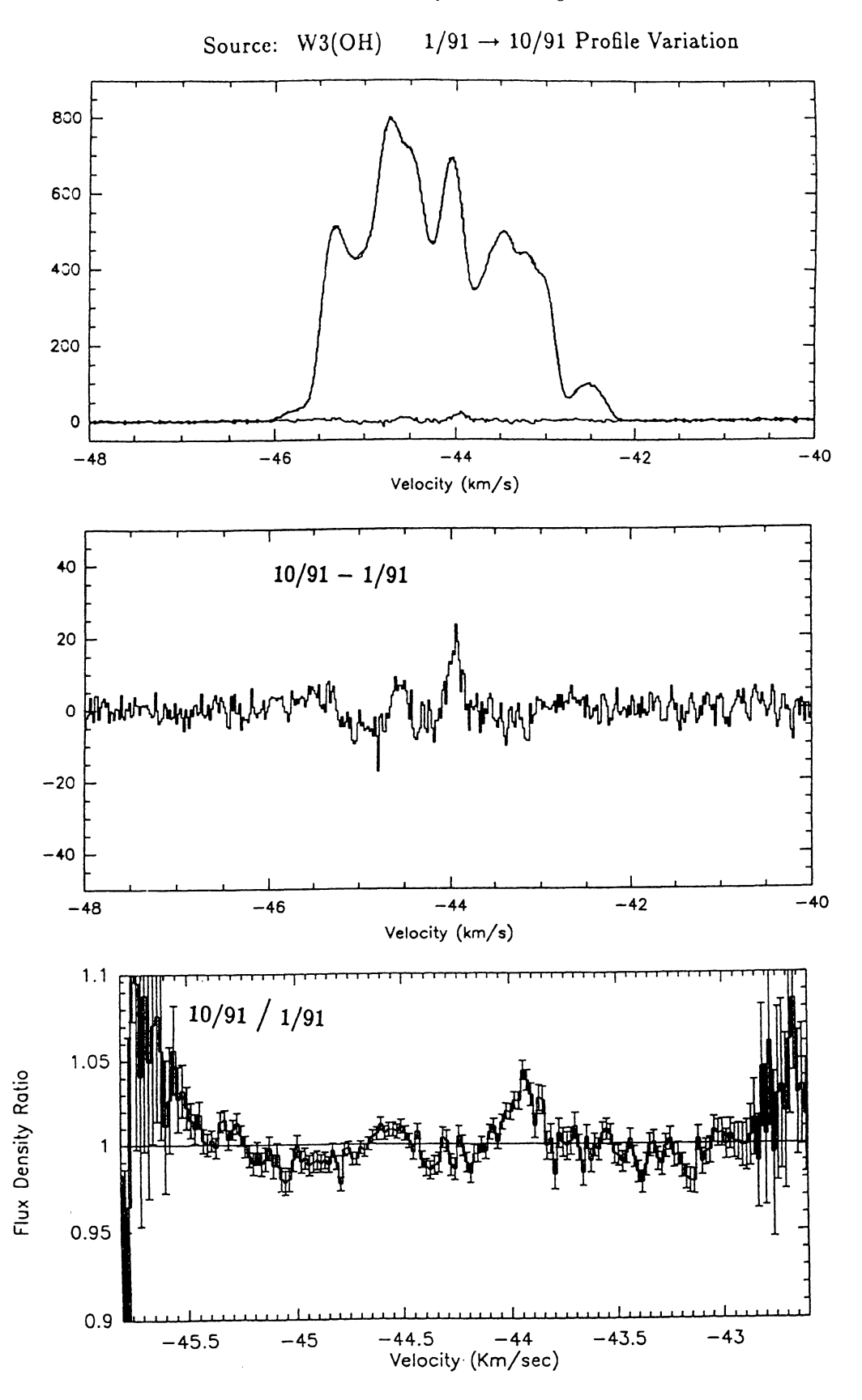


Fig. 5. b) The error bars of the flux density ratio plots correspond to the 1σ error. The flux density scale is in Jy. In Fig. 9a we give separately for the two emission intervals of W48 the plots of the best overlap between the spectra, of the residual and of the flux density ratio. In Fig. 9b (9c) we show the overlap of the spectral profiles of the first emission interval, on the top left, and the second emission interval, on the top right, when the residual of the first (second) emission interval is minimum. In the middle the residual for each of the two sections is shown. In the bottom we give the flux density ratio plot for the emission interval with the residual minimized (the first (second) one in Fig. 9b (9c))

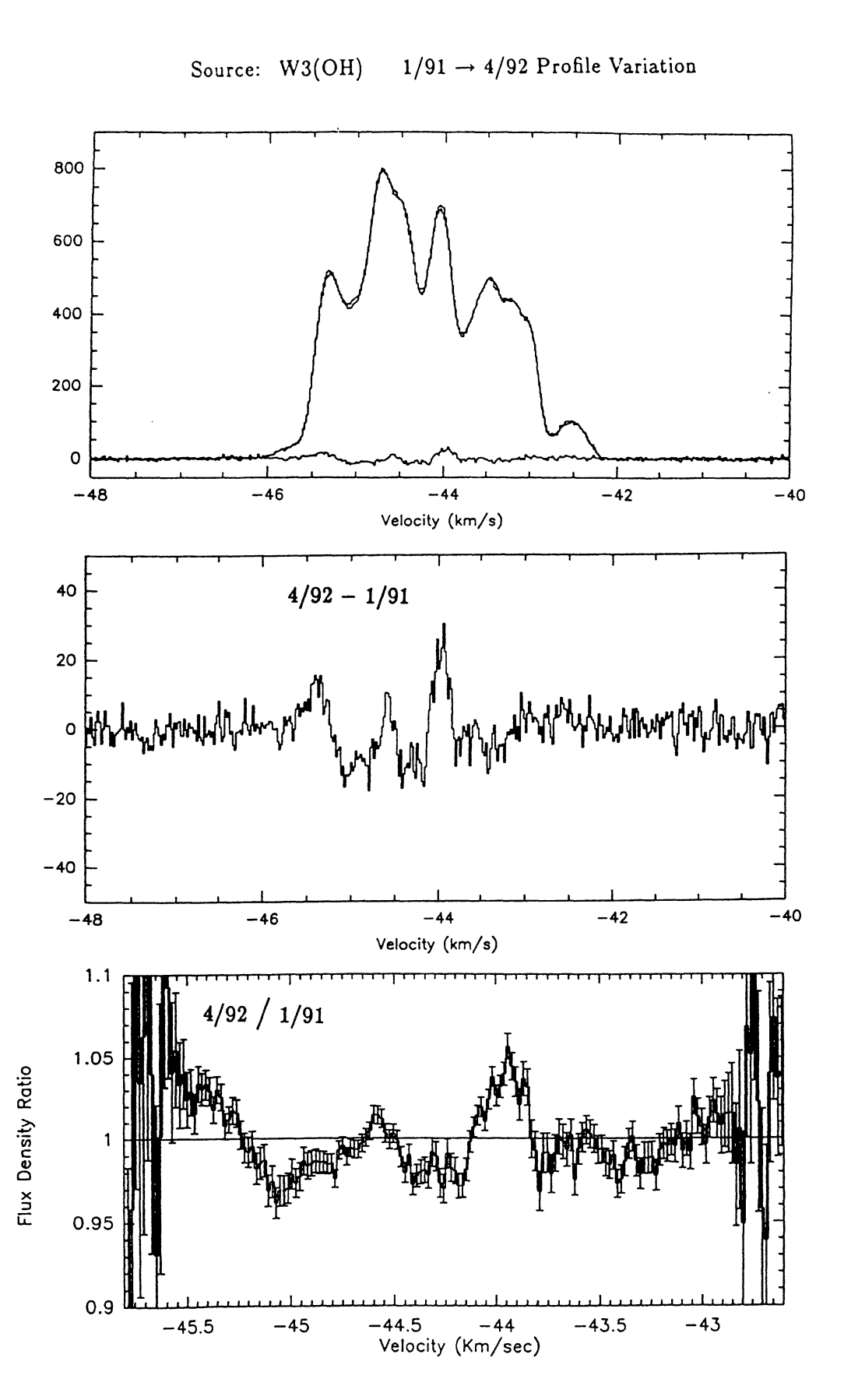


Fig. 5. c)

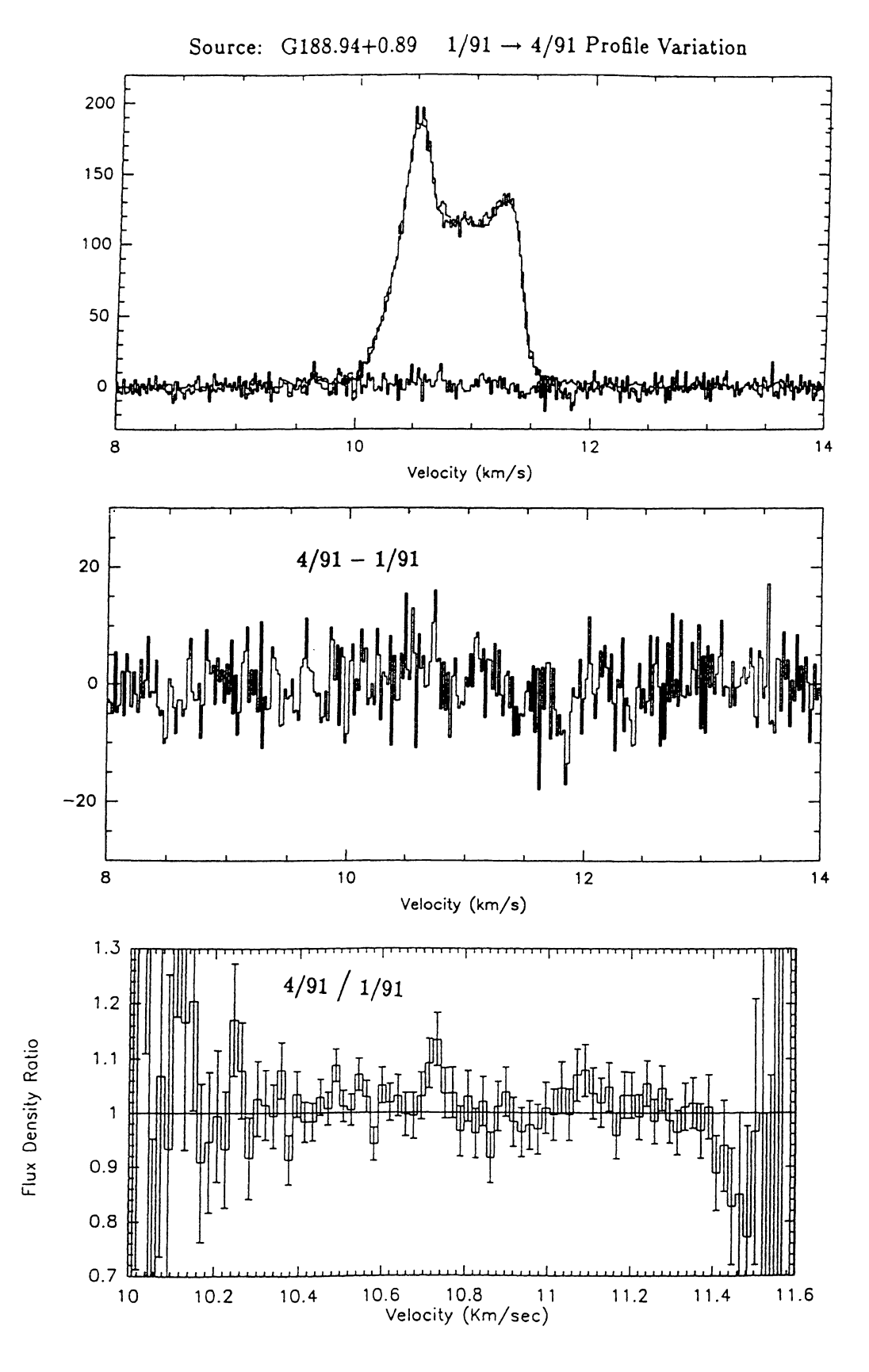


Fig. 6. a)

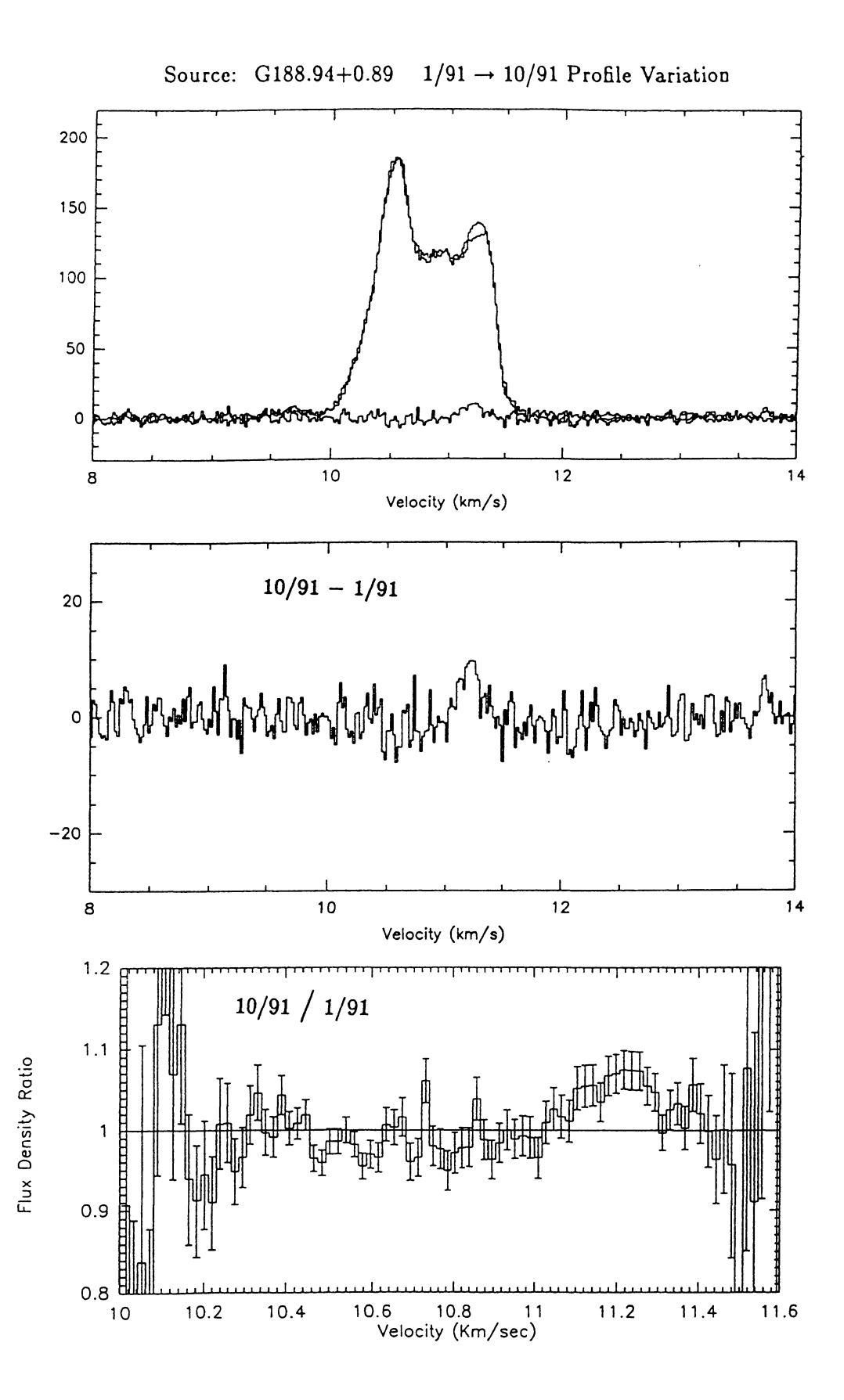
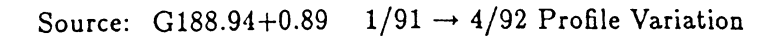


Fig. 6. b)



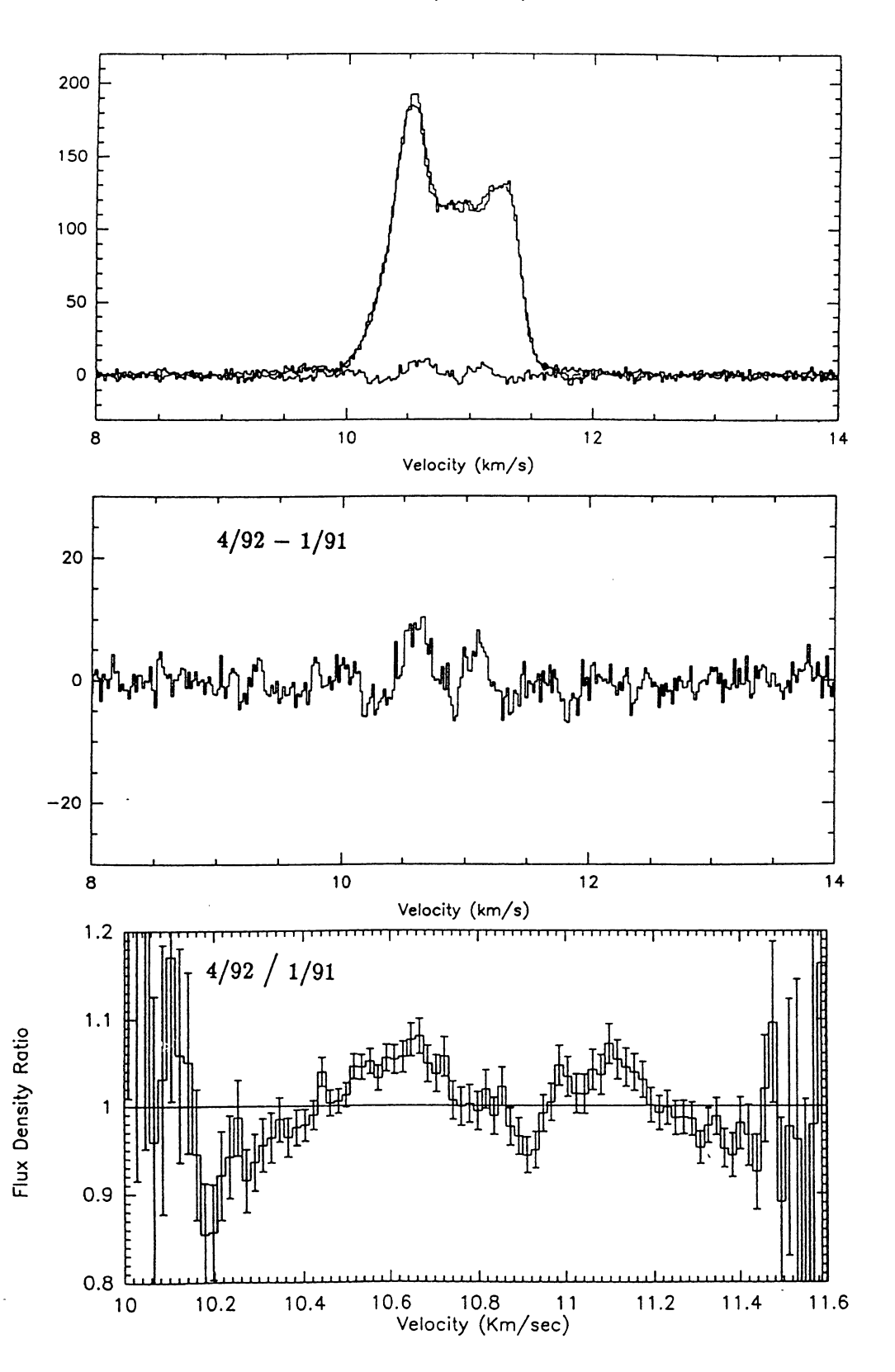


Fig. 6. c)

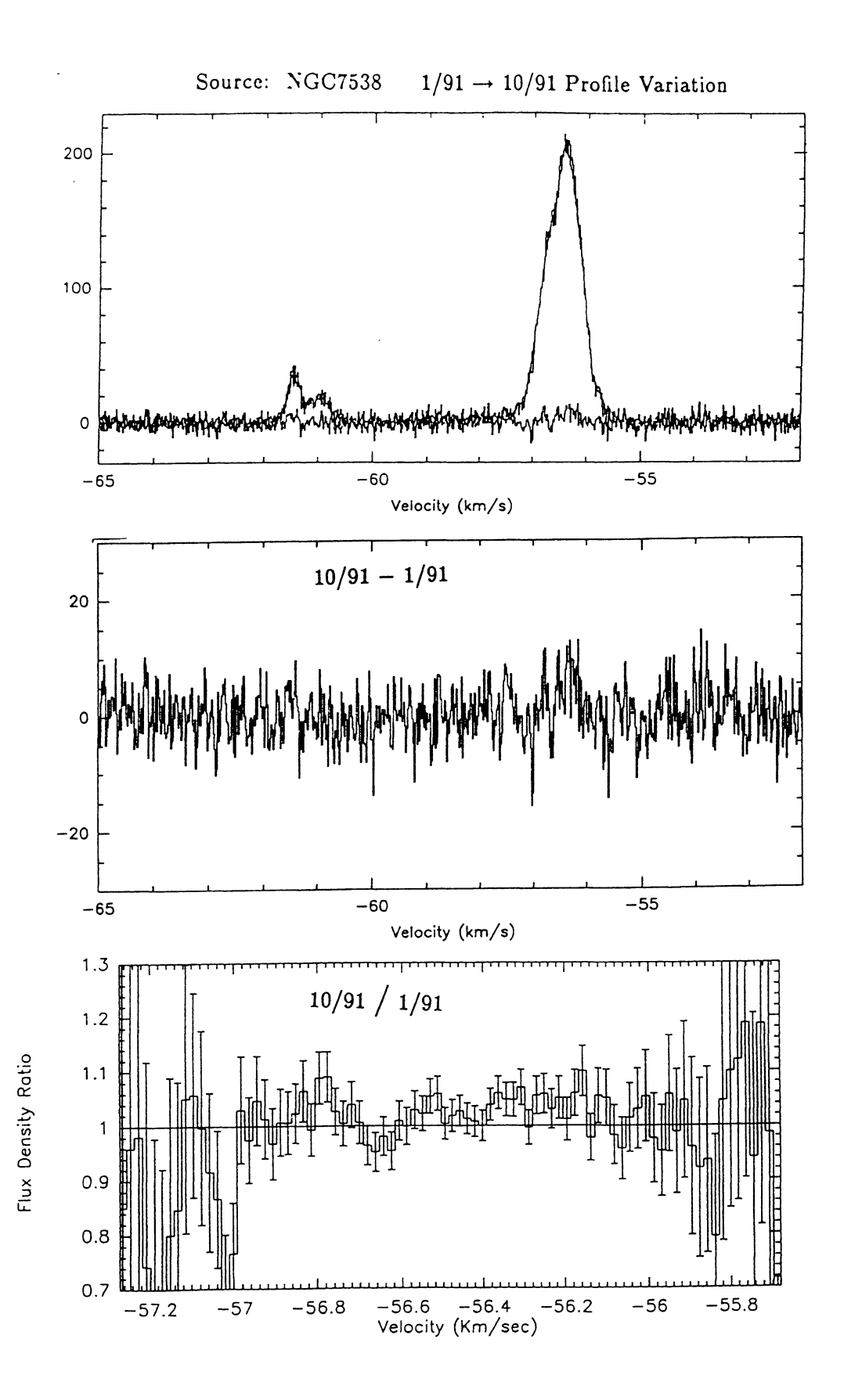
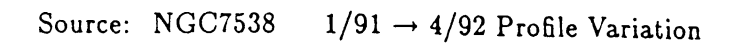


Fig. 7. a)

1996A&AS..116..211M

229



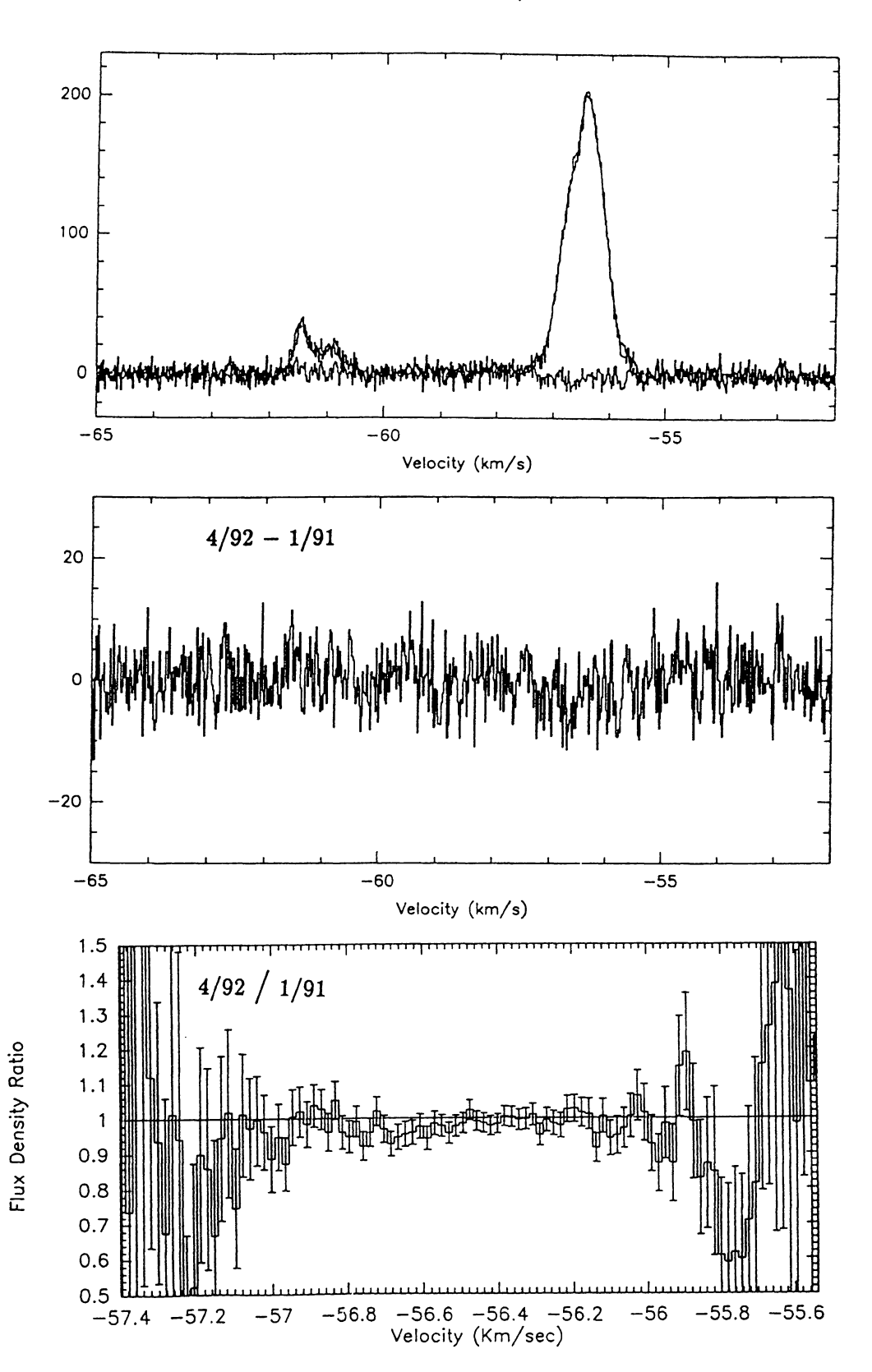


Fig. 7. b)

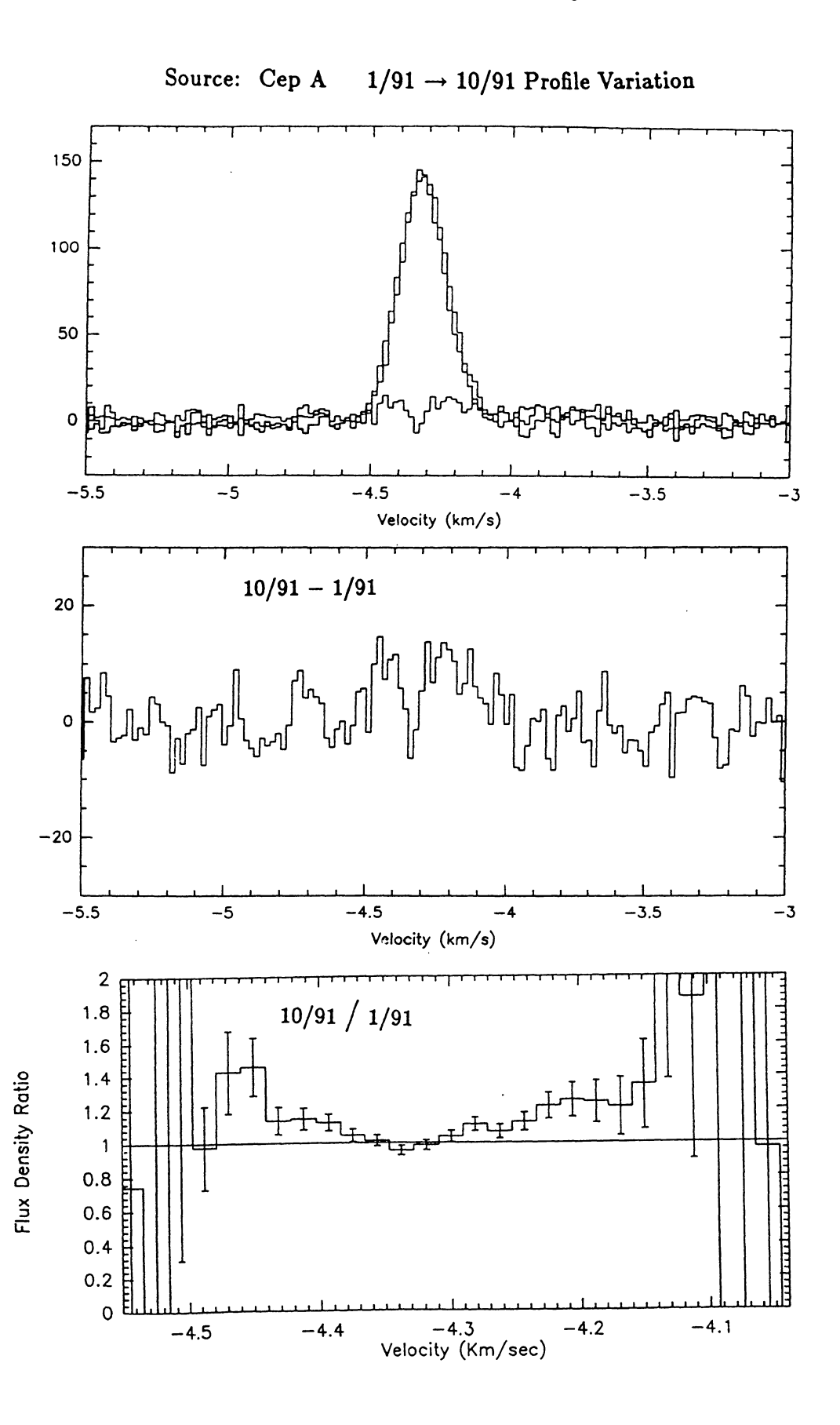


Fig. 8. a)

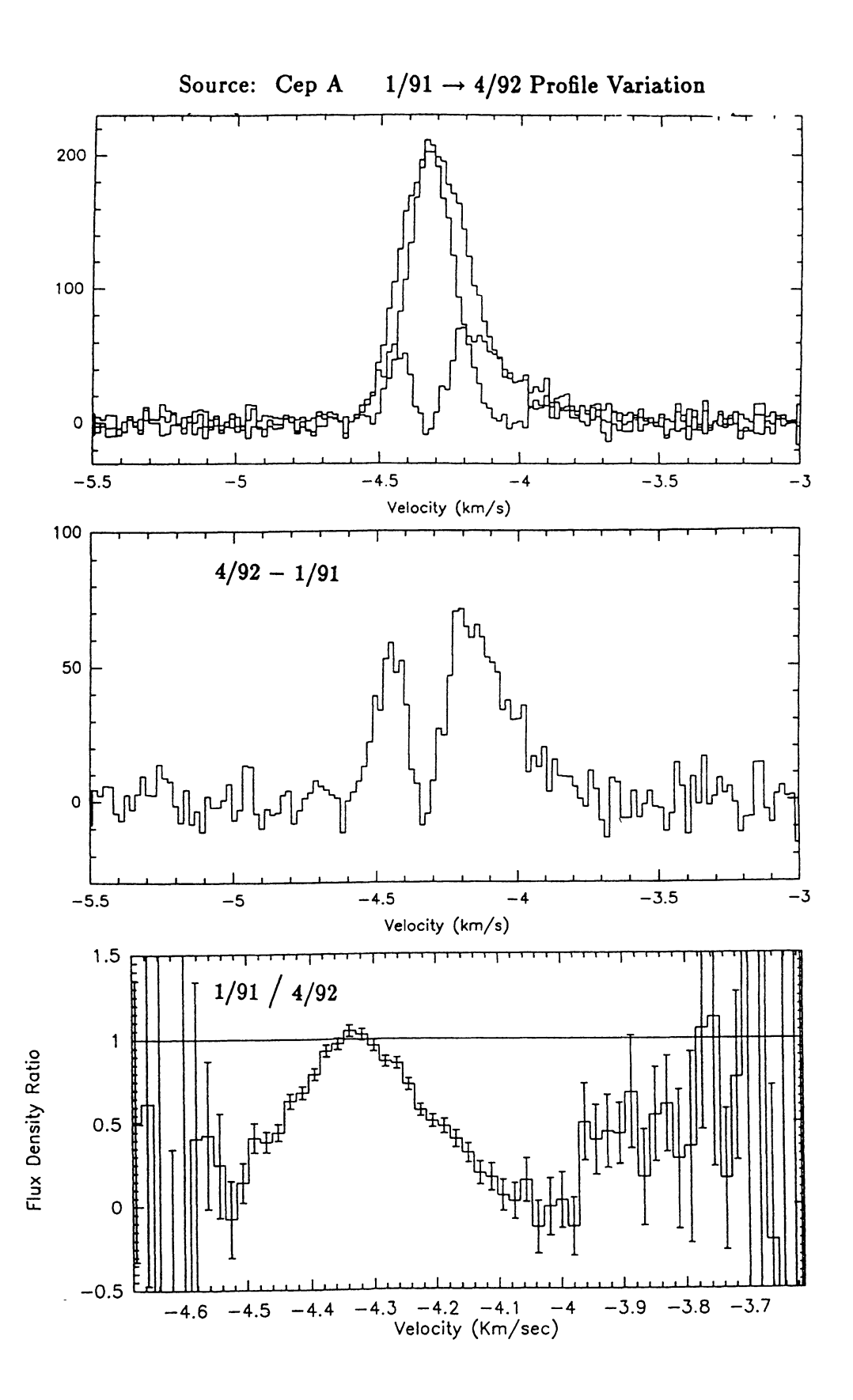


Fig. 8. b)



Source: W48 $1/91 \rightarrow 4/91$ Profile Variation

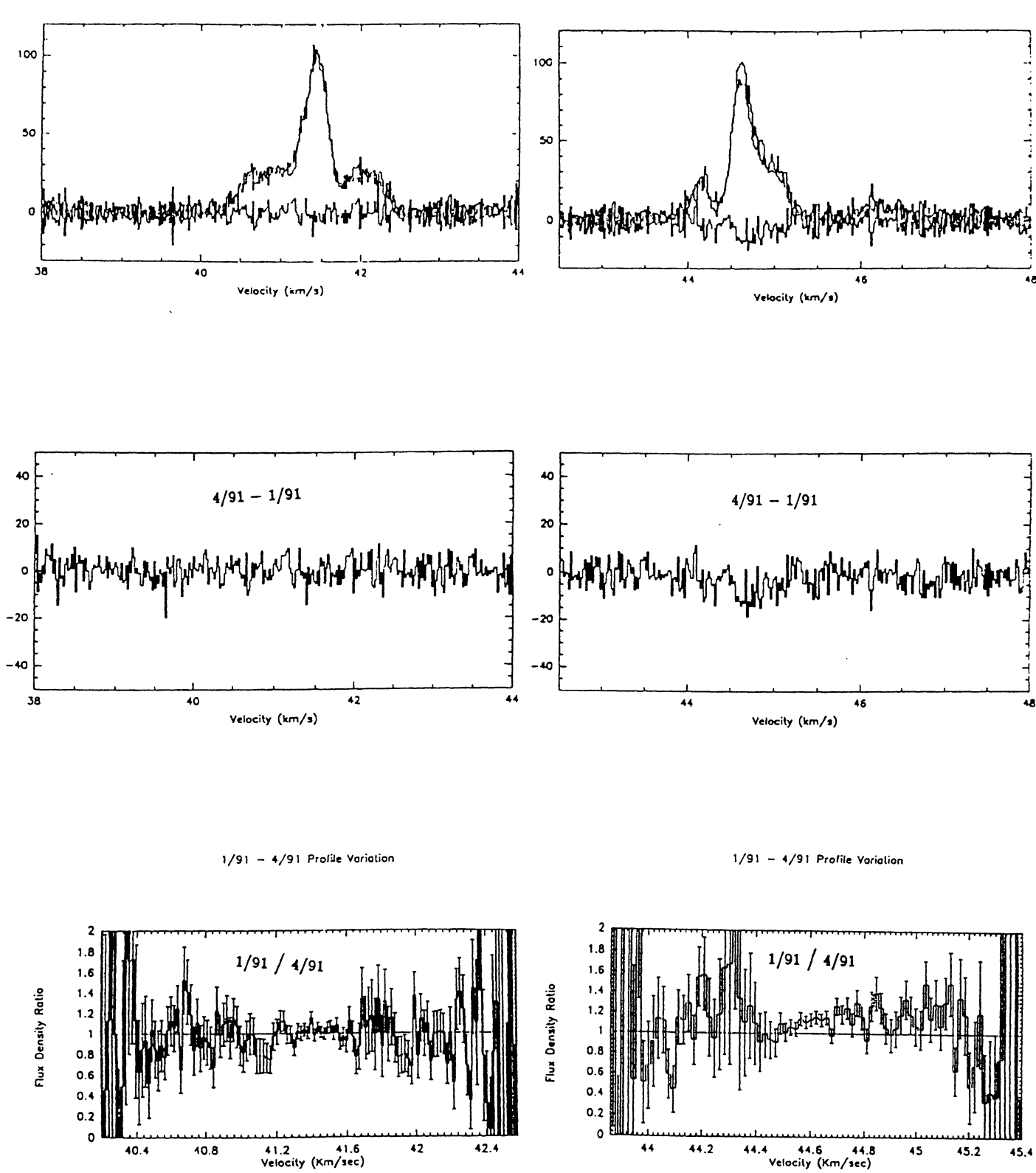


Fig. 9. a)

Source: W48 $4/91 \rightarrow 4/92$ Profile Variation

minimum residual for the 1° emission interval

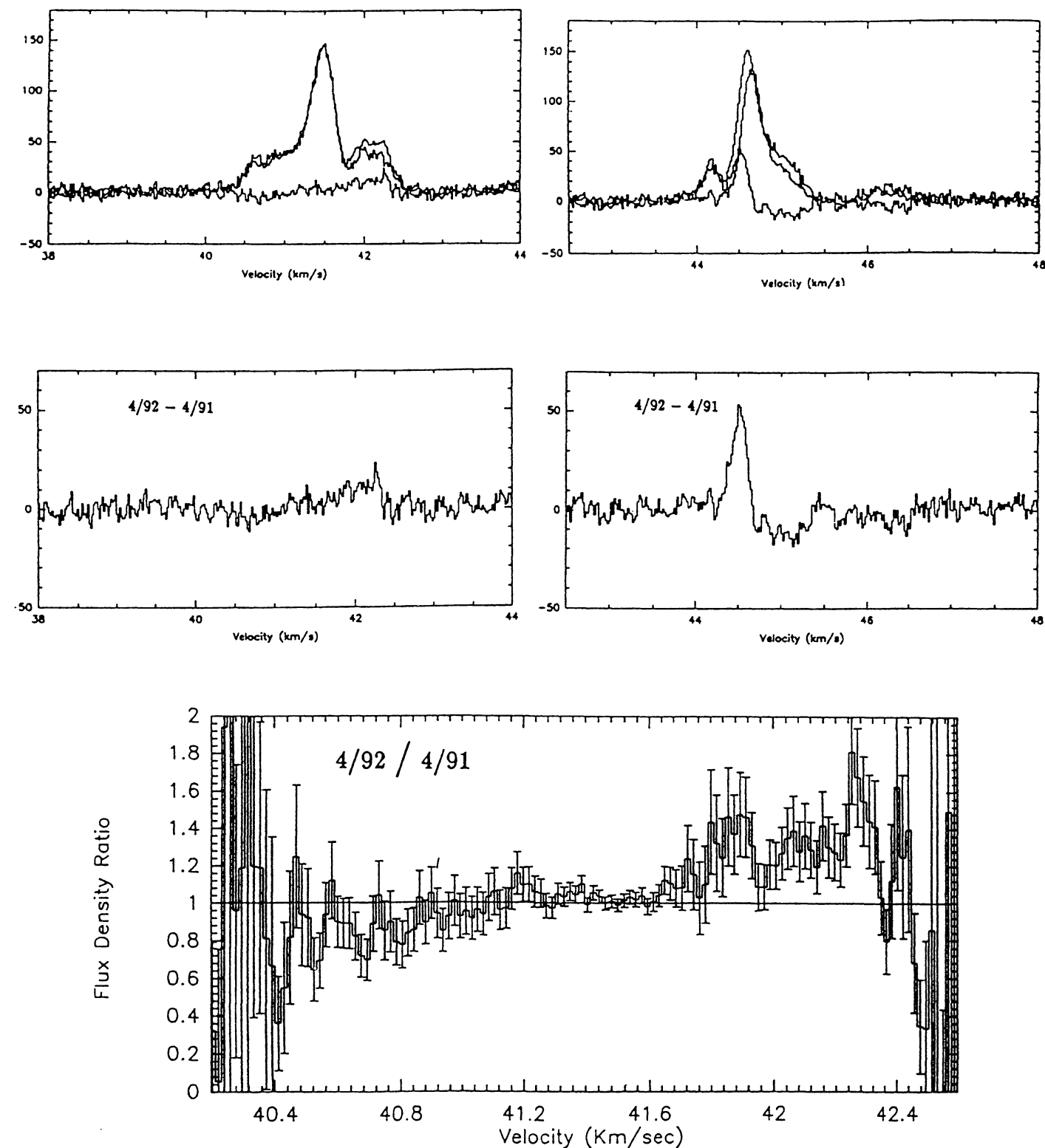


Fig. 9. b)

Source: W48 $4/91 \rightarrow 4/92$ Profile Variation

minimum residual for the 2° emission interval

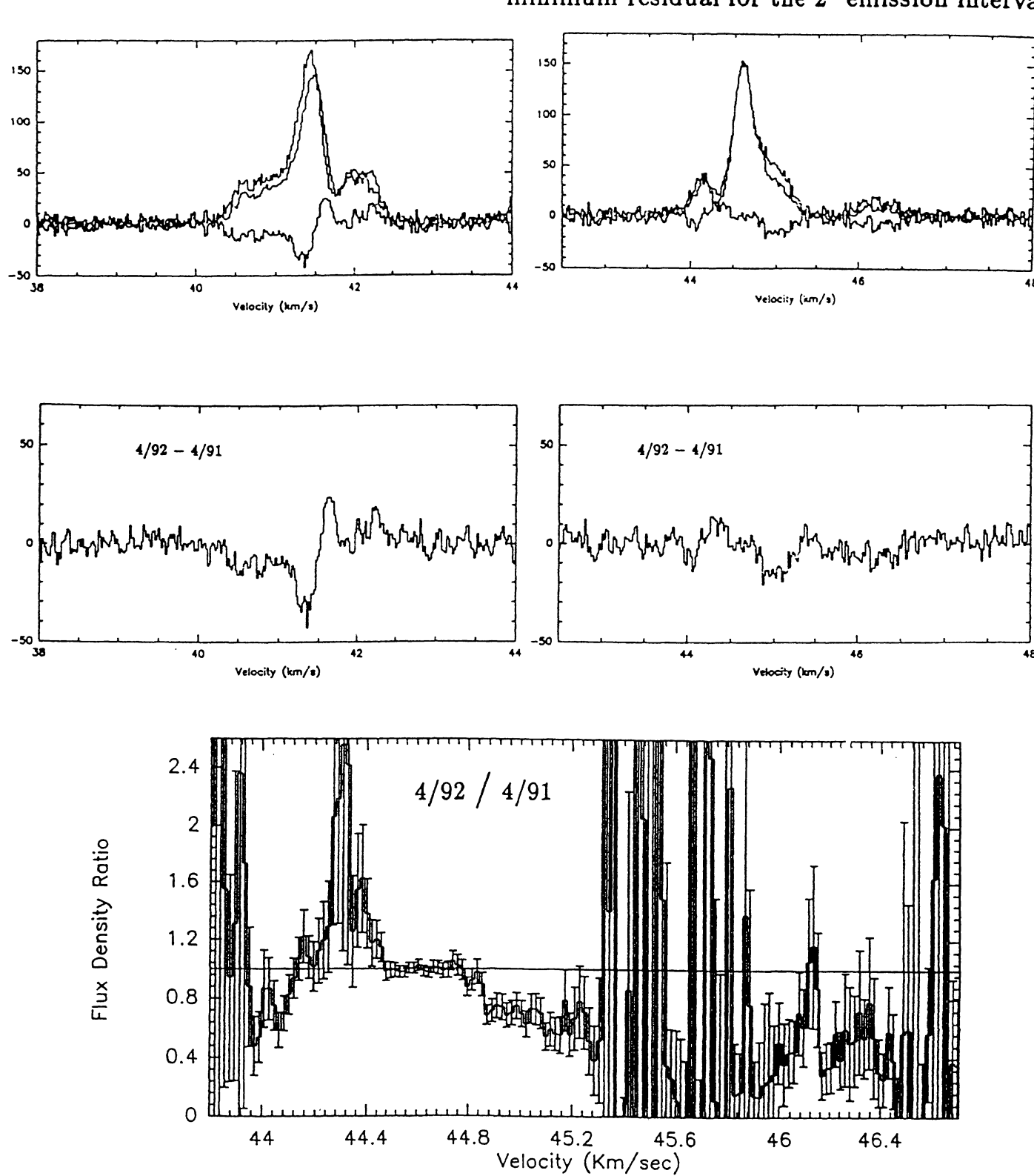


Fig. 9. c)

The nonuniform increase, respect to the velocity, of the intensity during the period 10/91-4/92 can be explained by assuming that the emission shows a different percentage of saturation with velocity: completely saturated at the peak, unsaturated in the wings. While the intensity of the saturated maser (the only one visible on 10/91) has continued to grow uniformly at all velocities, two new unsaturated features have appeared since then. So we interpret the two features present in the residual of the 1/91-4/92 comparison as the emission of two different maser spots, whose intensity has undergone an unsaturated growth during the period 10/91-4/92. The most intense of these ($\approx 65 \text{ Jy}$) at -4.17 km s^{-1} has a FWHM of $\approx 0.21 \text{ km s}^{-1}$, that is the thermal value, and therefore this maser feature has increased until becoming saturated. The other one is both weaker, ≈ 55 Jy, and narrower, \approx $0.13 \,\mathrm{km} \,\mathrm{s}^{-1}$, and it has still to reach the saturation threshold.

The origin of the time variability of the maser emission is mainly to be found in a modification of the pump rate and/or of the amplification path length. Between these two factors, it is more likely that it is the former to be determined globally (for all the maser spots) and therefore it can really be the common one responsible for the variability of both saturated and unsaturated maser spots. If these masers are radiatively pumped, as seems likely both from the observed vicinity of Class II methanol masers to radio and infrared continuum emission centers and from the results of pumping mechanism calculations, then the variation of the pump rate could be explained by a variation of the background (infrared) continuum radiation.

The only VLBI observation so far performed towards Cep A (Menten et al. 1988) determined the absolute position of the emission peak to be coincident with the continuum emission of the UCHII region 2 (Hughes et al. 1985). We have no information about the spatial distribution and the size of the various maser spots.

5) W48

In Table 8, the velocity and the flux density of the first and the second (in order of increasing velocity) emission peak are given for the mean spectrum of each run.

The mean integrated flux density of the first emission range, [39 km s⁻¹ - 43 km s⁻¹], is the same for the 1/91 and 4/91 runs (see Fig. 2). In agreement with our calibration criterion, we compare the mean spectra of the 1/91 and 4/91 runs without performing previously any amplitude normalization. The residual and the flux density ratio plots of Fig. 9a show that both the amplitude and the profile of the emission have not varied in both velocity intervals.

Because of the better signal-to-noise ratio, we use the 4/91 spectrum rather than the 1/91 one as reference to be compared with the 4/92 spectrum. The mean integrated flux density of the 4/91 and 4/92 runs is remarkably different, more than can be explained by calibration uncertain-

ties. So, to compare the profile of each of the two spectral sections, we first equalize the peak intensity. From our analysis it is evident that the velocity shift between the 4/91 and 4/92 mean spectra requested to minimize the residual is different for the two emission peaks. In Fig. 9b (9c) we show the overlap of the spectral profiles of the first emission interval, on the top left, and the second emission interval, on the top right, when the residual of the first (second) emission interval is minimum. In the middle the residual for each of the two intervals is shown. In the bottom, we present the ratio of the flux densities for the interval with the residual minimized. We find that in the 4/92 spectrum the peak separation is lower of $0.047\pm0.007~{\rm km~s^{-1}}$.

Furthermore, the two peaks present a slightly different rate of growth. In the 4/91 spectrum the ratio of the intensities of the first to the second peak is 1.12 ± 0.20 , while in the 4/92 spectrum it is 0.97 ± 0.08 (the errors are derived from the 3σ rms noise). The direct calculation of the ratio of the peak intensities between the two runs gives for the first peak, 1.47 ± 0.32 , for the second one, 1.70 ± 0.37 (in this case the errors are dominated by the calibration uncertainty).

For each peak we refer to the wing emission closer in velocity to the other peak as the "internal" wing (as located within the two peaks), whereas the other wing emission is refered as the "external" wing. For each of the two spectral sections the flux density ratio (in the bottom of Figs. 9b and 9c) shows that an asymmetric increase of the wings is present, with the internal one grown more than the external one. If one considers the whole emission range, the intensity increase is approximately symmetric with respect to the mid-point between the peaks, with the internal wings increased by a factor ≈ 1.3 more than the peaks, the external wings increased by a factor $\approx 1.2-1.3$ less than the peaks.

If we estimate the flux density limit for saturation of W48 using the same parameters as for Cep A, considering that the distance is larger by a factor of 4.4, we find a value about 20 times lower, $F_{\rm S}=3.5$ Jy. So we can reasonably assume that, for each epoch and at all velocities, the observed emission from W48 is saturated. This is confirmed by the fact that in the 1/91, 4/91 and 4/92 spectra, both peaks always have a costant and quite large FWHM (for the first one is ≈ 0.37 km s⁻¹, and for the second one ≈ 0.32 km s⁻¹). Therefore, both this estimate and the asymmetric growth of the wings around each peak, lets us exclude that a different percentage of saturation is the origin of the observed velocity dependence of the intensity increase.

The approximately symmetric appearance (in velocity) of the whole emission could derive from the particular spatial symmetry of the masering region. The spectrum emitted by an expanding (contracting) shell or a rotating disk (or torus) viewed edge-on should have three lines

Table 7. Velocity and intensity of the Cep A emission peak

Run	Peak		Peak		rms spectral noise	
	velocity	err.	intensity	err.		
	$({\rm km\ s^{-1}})$	$({\rm km\ s}^{-1})$	(Jy)	(Jy)	(Jy)	
1/91	-4.328	0.021	95.0	9.3	2.5	
10/91	-4.307	0.021	137.2	19.4	2.7	
4/92	-4.357	0.021	199.7	24.3	4.2	

Table 8. Velocity and intensity of the W48 emission peaks

	1° Peak		2° Peak		1° Peak		2° Peak		rms spectral
Run	velocity	err.	velocity	err.	intensity	err.	intensity	err.	noise
	$({\rm km~s}^{-1})$	$({\rm km~s^{-1}})$	$({\rm km\ s^{-1}})$	$(\mathrm{km}\;\mathrm{s}^{-1})$	(Jy)	(Jy)	(Jy)	(Jy)	(Jy)
1/91	+44.153	0.034	+44.328	0.021	102.0	10.6	99.6	10.5	4.6
4/91	+41.469	0.021	+44.661	0.021	98.3	9.3	88.0	8.5	2.8
4/92	+41.476	0.021	+44.612	0.021	144.4	17.5	149.4	18.1	2.9

(Cesaroni 1990), while ours always show only two peaks. However a rotating disk viewed edge-on can explain the observed dependence on velocity of the flux density ratio in the blue and red components better than an expanding (contracting) model. Assuming that the perturbation (shock or burst of radiation) responsible for the time variability showed, propagates through the whole inverted region in a negligible time compared with the light crossing time along the line of sight, whereas the emission increases almost synchronously in the whole inverted region, we see different origin (and velocity) photons arrive with a time delay that depends on the configuration. In the case of an expanding (contracting) model, we should see the flux density ratio of the blue (red) section decrease (increase) with velocity, contrary to what we observe. Instead, a rotating disk, assuming the rotation velocity is increasing with the radius, so that the emission at the most extreme velocities is generated by the most distant portions of the masering region, explains the observed behaviour of the flux density ratio in both the red and the blue spectral sections. The absence of the third emission peak, the one corresponding to the amplification path passing through the center of the disk, might be based on the fact that the thickness of the disk is much less that its size. This

one also agrees with our assumption that the propagation time of the perturbation is negligible compared with the light crossing time along the line of sight.

7. Conclusions

We have developed a technique of analysis to the study of minimal variations of the emission profile of methanol masers. The amplitude sensitivity is limited only by the spectral noise and it is possible to detect flux density variations as small as a few per cent.

Our results on W3(OH) and G188.94+0.89 show that even the very intense, probably saturated, 12 GHz methanol masers show a small rate of time variability, smoothly varying with the emission velocity. Over our 1.5 years period of observation, the maximum flux density variation is 6% for W3(OH) and 8% for G188.94+0.89. We interpret these very small variations as being due to proper motions of the maser spots.

The lower spectral signal-to-noise ratio limits our analysis of NGC 7538. We determine an upper limit for the variation of the flux density at any velocity over 1.5 years of 10%.

We observe a much higher variability in Cep A and W48. The emission peak of Cep A has increased by a factor

of 2.1 (\pm 0.46) during 1.5 years, while the analysis of the spectral profile shows that the emission in the wings has increased more than the peak. We interpret this as being due to the appearance of two unsaturated maser features.

The lower and higher velocity peaks of W48 have increased by a factor $1.47~(\pm~0.32)$ and $1.70~(\pm~0.37)$ respectively; in this case the wings around each peak show an asymmetric growth, with the internal wing increased more than the external one. Over the whole emission range the intensity increase is approximately symmetric with respect to the mid-point between the peaks, with the internal wings increased by a factor ≈ 1.3 more than the peaks, the external wings increased by a factor $\approx 1.2-1.3$ less than the peaks. This can be best interpreted in the frame of a rotating disk viewed edge-on.

Acknowledgements. We are very grateful to Jan Brand and Marcello Felli for critically reading the manuscript and for giving very helpful suggestions.

A. First moment error estimation

For a given source and run let us indicate with x(i) and $\sigma_{\rm ns}(i)$, i=1,N, respectively each measurement of the first moment of the emission velocity and the corresponding error (due only to the spectral noise and the velocity sampling).

In order to simplify the expressions we define the $\{\sigma(i)\}$ -weighting function, $\mathcal{W}(\{\sigma(i)\})$ ($\{\sigma(i)\}$) indicates the set $(\sigma(i) \ i = 1, N)$), and the variance function around \overline{x} , $\mathcal{D}(\overline{x})$, by means of:

$$W(\{\sigma(i)\}) = \frac{\sum_{i=1}^{N} x(i) / \sigma^{2}(i)}{\sum_{i=1}^{N} 1 / \sigma^{2}(i)^{2}}$$
(A1)

$$\mathcal{D}(\overline{x}) = \frac{\sum_{i=1}^{N} (x(i) - \overline{x})^2}{N - 1}$$
 (A2)

If we estimate the true value of the first moment with

$$\overline{x}_{\rm ns} = \mathcal{W}(\{\sigma_{\rm ns}(i)\}) \tag{A3}$$

then in most cases we find that the dispersion (the square root of the variance) of the measurements around \overline{x}_{ns} is higher or much higher than the root mean square of the errors:

$$\mathcal{D}(\overline{x}_{\rm ns}) \gg \frac{\sum_{i=1}^{N} \sigma_{\rm ns}^{2}(i)}{N}$$
 (A4)

We explain this by assuming that all the measurements are also affected by another kind of error, σ_{ir} (due to both instrumental factors and spectra reduction process), so that the effective error of the single measurement is given by:

$$\sigma_{\rm tot}(i) = \sqrt{\sigma_{\rm ns}^2(i) + \sigma_{\rm ir}^2}$$
 (A5)

Then the best estimate, \overline{x}_t , of the true value of the first moment is the $\{\sigma_{tot}(i)\}$ -weighted mean

$$\overline{x}_{t} = \mathcal{W}(\{\sigma_{tot}(i)\}) \tag{A6}$$

To determine the value of \overline{x}_t (or σ_{ir}) we assume that in correspondence of \overline{x}_t , otherwise than for \overline{x}_{ns} , the first and the second term of the relation A4 result effectively equal:

$$\mathcal{D}(\overline{x}_{t}) = \frac{\sum_{i=1}^{N} \sigma_{tot}^{2}(i)}{N} = \frac{\sum_{i=1}^{N} \sigma_{ns}^{2}(i)}{N} + \sigma_{ir}^{2}$$
(A7)

Note that for $\sigma_{\rm ir} \ll \sigma_{\rm ns}(i) \ \forall i$, we have $\overline{x}_{\rm t} \approx \overline{x}_{\rm ns}$, while in the opposite case, $\sigma_{\rm ir} \gg \sigma_{\rm ns}(i) \ \forall i$, we obtain $\overline{x}_{\rm t} \approx \overline{x}_{\rm a}$, the arithmetic mean. For any value of $\sigma_{\rm ir}$, $\overline{x}_{\rm t}$ is always between $\overline{x}_{\rm ns}$ and $\overline{x}_{\rm a}$. Let us consider the case, for istance, $\overline{x}_{\rm a} < \overline{x}_{\rm ns}$; then:

$$\overline{x}_{\rm a} < \overline{x}_{\rm t} < \overline{x}_{\rm ns}$$
 (A8)

The variance function $\mathcal{D}(x)$ has its minimum value for $x = \overline{x}_a$ and is always increasing for $x > \overline{x}_a$ and decreasing for $x < \overline{x}_a$. Therefore we can write:

$$\mathcal{D}(\overline{x}_{a}) < \mathcal{D}(\overline{x}_{t}) < \mathcal{D}(\overline{x}_{ns}) \tag{A9}$$

On the basis of the relation A7, we can use $\mathcal{D}(\overline{x}_{a})$ and $\mathcal{D}(\overline{x}_{ns})$ to obtain, respectively, a lower limit, $\sigma_{ir}(\overline{x}_{a})$, and an upper limit, $\sigma_{ir}(\overline{x}_{ns})$, estimate of σ_{ir} :

$$\sigma_{\rm ir}(\overline{x}_{\rm a}) < \sigma_{\rm ir} < \sigma_{\rm ir}(\overline{x}_{\rm ns})$$
 (A10)

If one uses $\sigma_{\rm ir}(\overline{x}_{\rm ns})$ to calculate $\overline{x}_{\rm t}$ by means of equations A5 and A6, one obtains a value located between $\overline{x}_{\rm a}$ and $\overline{x}_{\rm t}$, in our example, a lower limit estimate of $\overline{x}_{\rm t}$, indicated by $\overline{x}_{\rm t}^-$. On the other hand, using $\sigma_{\rm ir}(\overline{x}_{\rm a})$, one finds a value between $\overline{x}_{\rm ns}$ and $\overline{x}_{\rm t}$, or an upper limit estimate, $\overline{x}_{\rm t}^+$. Therefore:

$$\overline{x}_{t}^{-} < \overline{x}_{t} < \overline{x}_{t}^{+} \tag{A11}$$

The procedure can be iterated until the required approximation has been reached, i.e., until the difference between the upper and the lower limit estimate of \overline{x}_t is negligible compared to the dispersion of the measurements around both estimates. In all cases this occurs already at the first step of the iteration. So we evaluate \overline{x}_t by means of the arithmetic mean between \overline{x}_t^- and \overline{x}_t^+

$$\overline{x}_{t} = \frac{\overline{x}_{t}^{+} + \overline{x}_{t}^{-}}{2} \tag{A12}$$

and estimate the corresponding error σ_t by means of the dispersion of the measurements around \overline{x}_t

$$\sigma_{\rm t} = \sqrt{\mathcal{D}(\overline{x}_{\rm t})}$$
 (A13)

References

Batrla W., Matthews H.E., Menten K.M., Walmsley C.M., 1987, Nat 326, 49

Bloemhof E.E., Reid M.J., Moran J.M., 1992, ApJ 397, 500 Caswell J.L., Gardner F.F., Norris R.P., et al., 1993, MNRAS 260, 425

Catarzi M., Curioni P., Curioni G.P., et al., Arcetri Tech. Rep. 1/1990

Catarzi M., Moscadelli L., Panella D., 1993, A&AS 98, 127 Cesaroni R., 1990, A&A 233, 513

Cesaroni R., Walmsley C.M., 1991, A&A 241, 537

Cragg D.M., Johns K.P., Godfrey P.D., Brown R.D., 1992, MNRAS 259, 203

Crampton D., Georgelin Y.M., Georgelin Y.P., 1978, A&A 66, 1

Downes D., Wilson T.L., Bieging J., Wink J., 1980, A&AS 40, 379

Forster J.R., Caswell J.L., Okumura S.K., Hasegawa T., Ishiguro M., 1990, A&AS 231, 473

Garmany C., 1973, ApJ 78, 185

Hughes V.A., 1985, ApJ 298, 830

Humphreys R.M., 1978, ApJS 38, 309

Kompe C., Joncas G., Baudry A., Wouterloot J.G.A., 1989, A&AS 221, 295

Koo B.C., Williams D.R.W., Heiles C., Backer D.C., 1988, ApJ 326, 931

Kurtz S., Churchwell E., Wood D.O.S., 1993 (in press in ApJS) Lees R.M., 1973, ApJ 184, 763

MacLeod G.C., Gaylard M.J., Nicolson G.D., 1992, MNRAS 331, L37

MacLeod G.C., Gaylard M.J., Kemball A.J., 1993, MNRAS 262, 343

Menten K.M., Reid M.J., Moran J.M., 1988, ApJ 333, L83 Menten K.M., 1991a, in: Haschick A.D. & Ho P.T.P. (eds.) Proc. Third Haystack Obs. Meeting, "Skylines", Astron.

Soc. Pacif., San Francisco, p. 119

Menten K.M., 1991b, ApJ 380, L75Menten K.M., Reid M.J., Pratap P., Moran J.M., Wilson T.L., 1992, ApJ 401, L39

Norris R.P., McCutcheon W.H., Caswell J.L., et al., 1988, Nat 335, 149

Ott M., Witzel A., Quirrenbach A., et al., 1994, A&A 284, 331 Van Buren D., Mac Low M.M., Wood D.O.S., Churchwell E., 1990, ApJ 353, 570